Digital-Based Potentiostat and Mesoporous Microelectrode Co-Design for Non-Enzymatic Glucose Detection at 0.3V- VDD and 1.65nW-Power

Digital-Based Potentiostat and Mesoporous Microelectrode Co-Design for Non-Enzymatic Glucose Detection at 0.3 V-V_{DD} and 1.65 nW-Power

Andrea De Gregorio, Mara Serrapede, Danilo Kaddouri, Paolo Angelini, Giuseppe Bruno, Simone Luigi Marasso, Salvatore Guastella, Andrea Lamberti, and Paolo Crovetti, *Senior Member, IEEE*

***Abstract*—This paper presents a proof-of-concept ultra-low-voltage and ultra-low-power chronoamperometric sensing platform for non-enzymatic glucose detection, based on the co-design of a reconfigurable digital-based (DB) potentiostat and a mesoporous platinum (Pt) microelectrode. The DB potentiostat enables current readout and direct digitization from a 0.3 V supply at nanowatt-level power, while the microelectrode geometry and mesoporous Pt nanostructuring provide non-enzymatic glucose sensitivity at physiologically relevant concentrations within an electrochemical operating window compatible with the voltage and power constraints of the readout. A frequency-domain signal and noise model of the DB potentiostat is derived for the first time and validated through simulations and measurements, providing a quantitative basis for the electrochemical/readout co-design. Fabricated in 130 nm CMOS, the DB potentiostat achieves 5.6 pA_{rms} input-referred noise, corresponding to a 16.8 pA circuit-level minimum detectable current, while consuming 1.65 nW at V_{DD}=0.3 V. Electrochemical currents from 600 pA to 650 nA are experimentally measured with R^2=0.991 linearity under ferrocyanide test conditions. Non-enzymatic glucose measurements with mesoporous Pt microelectrodes at physiologically relevant concentrations, under aerobic conditions and with ascorbic acid as an interferent, demonstrate, to the best of the authors' knowledge, the lowest reported power consumption for CMOS non-enzymatic glucose readout, supporting the potential of the proposed platform for emerging point-of-care diagnostics applications.**

***Index Terms*—Digital-based (DB) potentiostat, digital operational transconductance amplifier (DIGOTA), ultra-low power (ULP), ultra-low voltage (ULV), electrochemical current sensing, microelectrodes, non-enzymatic glucose detection.**

Andrea De Gregorio and Paolo Crovetti are with the Department of Electronics and Telecommunication (DET), Politecnico di Torino, 10129 Turin, Italy (emails: andrea.degregorio@polito.it, paolo.crovetti@polito.it)
Mara Serrapede, Simone Luigi Marasso, Salvatore Guastella and Andrea Lamberti are with the Department of Applied Science and Technology (DISAT), Politecnico di Torino, 10129 Turin, Italy (emails: mara.serrapede@polito.it, simone.marasso@polito.it, salvatore.guastella@polito.it, andrea.lamberti@polito.it)
Danilo Kaddouri, Paolo Angelini and Giuseppe Bruno are with STMicroelectronics, Milan, Italy (email: danilo.kaddouri@st.com, paolo.angelini@st.com, giuseppe.bruno@st.com)
This publication is part of the project PNRR-NGEU which has received funding from MUR - DM 117/2023. This study was carried out within the MicroBioNIC project within the PRIN 2022 program, CUP: E53C24002620006 (D.D. 104 - 02/02/2022 Ministero dell'Università e della Ricerca). This manuscript reflects only the authors' views and opinions and the Ministry cannot be considered responsible for them. This work was partially funded under the National Recovery and Resilience Plan (NRRP), Mission 4 "Education and Research"-Component 2 "From research to business"- Investment 3.1 "Fund for the realization of an integrated system of research and innovation infrastructures"- Call for tender No. N. 3264 of 28/12/2021 of Italian Ministry of Research funded by the European Union-NextGenerationEU Project code: IR0000027, Concession Decree No. 128 of 21/06/2022 adopted by the Italian Ministry of Research, CUP: B33C22000710006, Project title: iENTRANCE.

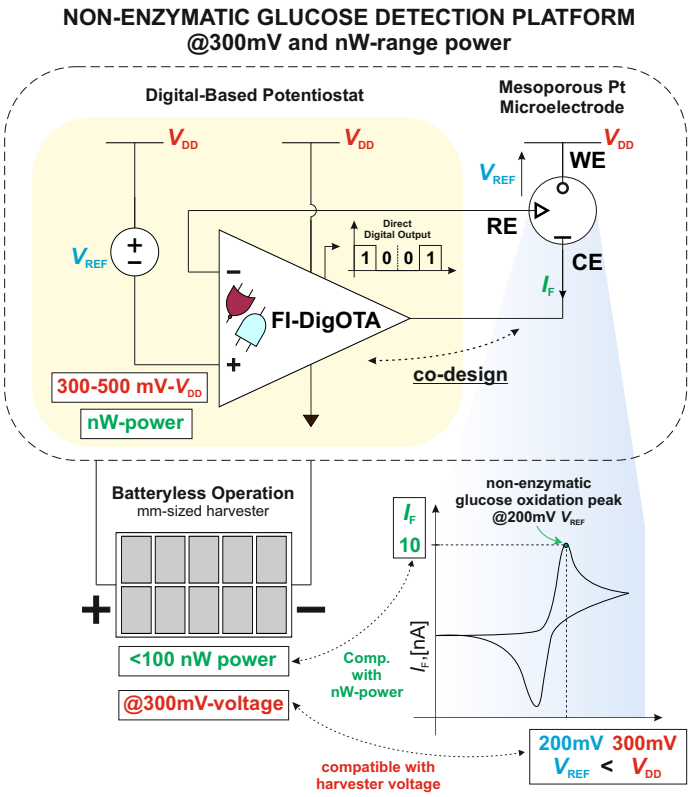

Fig. 1: Electrochemical-biosensor constraints for non-enzymatic glucose detection addressed by the proposed DB potentiostat and mesoporous platinum (Pt) microelectrode co-design.

I. Introduction

EMERGING wearables, personalized healthcare and point-of-care (PoC) diagnostics require robust, untethered, energy-autonomous electrochemical sensing platforms capable of delivering reliable real-time information on the concentration of clinically relevant analytes such as glucose, lactate and drugs [1] [2] [3] [4] [5].

Meeting such requirements in electrochemical sensors results in many challenges both in the design of the sensing electrodes and in the readout integrated circuits (ICs), that need to be addressed in a synergistic way [6].

At the sensor level, conventional electrochemical sensors that take advantage of enzyme-mediated reactions to enhance selectivity are not attractive due to their stringent limitations in operating and storage conditions, potential enzyme instability, dependence on cofactors and stabilizers and susceptibility to interferents [7] [8] [9]. At the readout level, energy autonomous sensing platforms demand integrated circuits operating at ultra-low voltage (ULV) and ultra-low power (ULP) consumption (up to tens of nW) to be supplied by an unregulated energy harvester or to maximize the lifetime of miniaturized batteries [10] [11].

Aiming to overcome the limitations of enzymatic sensing, non-enzymatic electrochemical biosensors enabling direct oxidation or reduction of the analyte at the electrode surface have been proposed and investigated for decades [2] [3] [4] [5] [8] [9] [12]. Among these materials, platinum (Pt) and Pt-based composites are widely used due to their excellent electrocatalytic activity toward small biomolecules, high conductivity, chemical stability under physiological conditions, and general biocompatibility [4] [5] [7] [8] [9]. Consequently, significant efforts have focused on engineering Pt nanostructures and surface chemistries to boost catalytic efficiency, lower overpotentials, and enhance resistance to interferents [2] [3] [4] [5] [8] [9] [12].

From the IC readout point of view, conventional potentiostats for amperometric readout, based on current-to-voltage conversion by resistive [13] [14] [15] [16] or capacitive [17] [18] [19] [20] [21] feedback transimpedance amplifiers (TIA) and analog-to-digital converters (ADCs), often require impractically large passives and/or low noise, high performance amplifiers which are not compatible with low voltage and low power operation. Alternatives based on current conveyors (CCs) [22] [23] [24] [25] extend the input range at the cost of a further increased power consumption and, solutions based on current-to-frequency conversion [26] [27] [28], enable the direct digitization of the sensed currents without external ADCs but often require high-speed comparators and counters, resulting in marginal power savings.

More recently, wide dynamic range and nW-power operation have been demonstrated in digital-based (DB) potentiostats [29] [30]. In details, DB potentiostats [29] [31] [32] inherit the advantages of the digital operational transconductance amplifier (DIGOTA) [33] [34] and of the floating inverter (FI)-based DIGOTA (FI-DIGOTA) [29] [31] and achieve both ULV and ULP operation, thanks to bias current suppression, near-threshold dynamic biasing, and direct digitization without external ADCs.

The electrochemical sensors proposed so far for non-enzymatic glucose monitoring, however, typically require electrochemical operating voltages well above the minimum supply voltage of a DB potentiostat, i.e., 300 mV, while standard centimeter-sized electrodes generate faradaic currents in the tens-of-microamperes range. This keeps the minimum readout supply voltage above 1 V and the power consumption in the tens-of-microwatts range, thereby limiting the inherent advantages of the digital-based approach.

This paper proposes a proof-of-concept ULV/ULP amperometric sensing platform for non-enzymatic glucose detection, in which a DB potentiostat and a nanostructured mesoporous platinum microelectrode are co-designed to bring glucose readout into the 0.3 V, nanowatt-power regime. The DB potentiostat performs direct current digitization from a 0.3 V supply at nanowatt-level power, while the mesoporous Pt microelectrode, fabricated according to the method first proposed by Attard et al. [35], provides a high-surface-area microscale electrochemical interface that yields nA-range faradaic currents at physiologically relevant glucose concentrations within a sub-300 mV electrochemical operating window. This places the glucose signal within the current-resolution and voltage-headroom limits of the DB readout, as summarized in Fig. 1.

The contributions of this work are threefold. First, a frequency-domain signal and noise model of the DB potentiostat is developed and validated, providing a quantitative description of current-to-digital conversion, noise shaping and input-referred current resolution. Second, the work demonstrates an electrochemical/readout co-design route for non-enzymatic glucose detection in the 0.3 V, nanowatt-power regime. Third, the platform is validated along a progressive experimental path: electrical characterization of the DB potentiostat, electrochemical characterization with ferrocyanide as a standard redox probe, and proof-of-concept non-enzymatic glucose measurements at physiologically relevant concentrations under aerobic conditions and with ascorbic acid as an interferent.

The rest of the paper is organized as follows. Sect.II briefly revisits the FI-DIGOTA architecture and its operation as a DB potentiostat. Sect.III develops, for the first time, an equivalent frequency-domain linearized model that analytically describes the signal-transfer and noise behavior of the DB potentiostat and validates it through simulations and measurements. Sect.IV describes the design and fabrication of the mesoporous Pt microelectrodes, together with the electrochemical/readout co-design of the proposed sensing platform. Sect.V reports the electrical characterization of the DB potentiostat. Sect.VI validates the electrochemical readout through ferrocyanide oxidation-current measurements, used as a standard redox-probe test. Sect.VII demonstrates the proof-of-concept operation of the complete platform for non-enzymatic glucose sensing under aerobic conditions and with ascorbic acid as an interferent. Finally, Sect.VIII draws the conclusions of the paper.

II. The FI-DIGOTA Circuit

To bring non-enzymatic glucose readout into the 0.3 V, nanowatt-power regime, this work adopts the FI-DIGOTA-based DB potentiostat shown in Fig. 2. The architecture builds on the DB potentiostat topology originally proposed in [29] and later adapted for dopamine sensing in [32].

This section briefly recalls the FI-DIGOTA operating principle, including the configurable output stage described in [31], and its open-loop frequency-domain representation, following the modeling approach in [34]. This representation is then used in Sect. III to derive the signal and noise transfer functions of the DB potentiostat in feedback with the electrochemical cell.

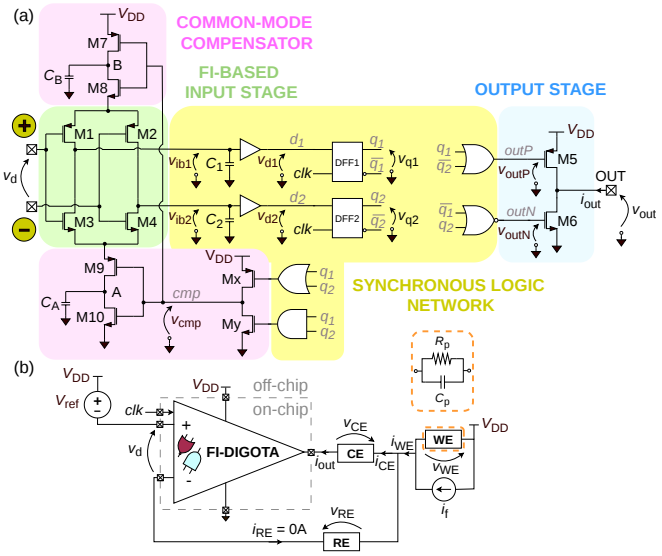

Fig. 2: (a) FI-DIGOTA circuit schematic, (b) DB potentiostat: FI-DIGOTA in feedback with an electrochemical cell.

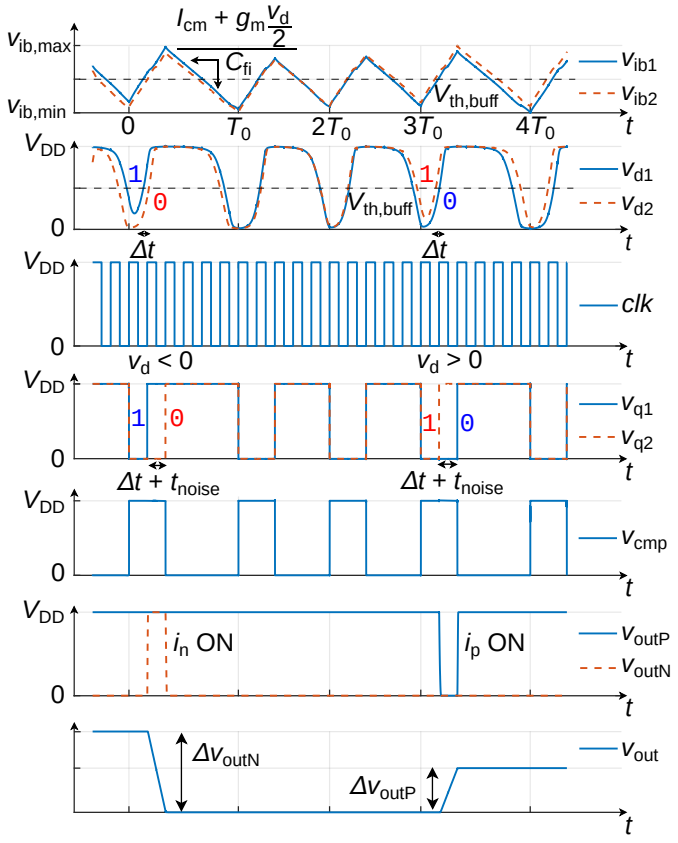

Fig. 3: FI-DIGOTA internal waveforms.

A. Architecture and Operating Principle

The FI-DIGOTA in Fig. 2a comprises a floating inverter (FI) based input stage (M1 – M4), a synchronous logic network, a common mode (CM) compensation network (Mx, My, M7 – M10) and a three-state output stage (M5 – M6). In the proposed implementation, the strength of the nMOS and pMOS devices of the output stage can be independently configured by two 8-bit digital calibration words [31].

The behavior of the internal waveforms of the circuit is depicted in Fig. 3. The outputs of the FI-based input stage ($v_{\rm ib1}$, $v_{\rm ib2}$) are converted into two-level signals $v_{\rm d1}$ and $v_{\rm d2}$ by comparison with the threshold voltages $V_{\rm th,buff}$ of two digital buffers. These signals are then sampled by two D-type flip-flops (D-FFs), resulting in four possible states for (q_1, q_2): (0,0), (0,1), (1,0), and (1,1).

According to the algorithm described in [33] [34], when q_1 and q_2 assume the same logical value, the sign of the differential input voltage $v_{\rm d}$ cannot be inferred and the CM compensation network is activated to provide dynamic biasing to the FI input stage. If $q_1 = q_2 = 0$ ($q_1 = q_2 = 1$) the positive (negative) supply of the input stage is connected through M8 (M9) to the capacitance $C_{\rm B}$ ($C_{\rm A}$), that was pre-charged at $V_{\rm DD}$ (0V) via M7 (M10). On the other hand, if $q_1 = 0$ and $q_2 = 1$ ($q_1 = 1$ and $q_2 = 0$), a positive (negative) $v_{\rm d}$ can be inferred and the pMOS M5 (nMOS M6) is turned on to sink (source) current to (from) the load.

In the absence of a differential input component, the FI-DIGOTA operates in a self-oscillating mode, periodically switching between (0,0) and (1,1) states, with a self-oscillation period (T_0) dependent on the charge/discharge rate of the parasitic output capacitors (C_1, C_2) of the FI, as detailed in [34]. A nonzero differential input can be modeled as a perturbation superimposed on the steady-state oscillation, that gives rise to opposite variations in the charging slopes $v_{\rm ib1}$ and $v_{\rm ib2}$, resulting in a timing difference (Δt in Fig. 4a) between the switching events of the digital buffers proportional to the input differential voltage $v_{\rm d}$. Unlike in the architecture in [34], the D-FFs sample the buffer output voltages $v_{\rm d1}$ and $v_{\rm d2}$, thus effectively quantizing Δt into integer multiples of the clock period and driving the output stage by synchronous digital output streams $outP$ and $outN$.

B. FI-DIGOTA Frequency Response

The frequency-domain analysis of the FI-DIGOTA adapts the modeling approach in [34] to account for two differences: the FI-based rather than Muller-C input stage and the synchronous rather than asynchronous operation.

Under the same assumptions in [34], both DIGOTA and FI-DIGOTA can be described as the cascade connection of an equivalent transconductance input stage followed by a voltage-to-time conversion block, which converts the input differential voltage into a proportional timing difference Δt and by a time-to-current conversion block, that converts Δt into current pulses driving an RC output impedance, as shown in Fig. 4a.

Although the Muller-C input stage in [34] and the FI- based input stage considered in this work are different, under small-signal conditions, the perturbation in their output currents related to the input differential voltage can be described in both cases in terms of a time-varying transconductance, whose averaged value is fairly constant over each CM-compensation cycle, that drives an equivalent RC load representing the output resistance of the FI stage $r_{\rm o}$ in parallel to the parasitic capacitance $C_{\rm fi}$ at the FI output node, resulting in a one-pole transfer function.

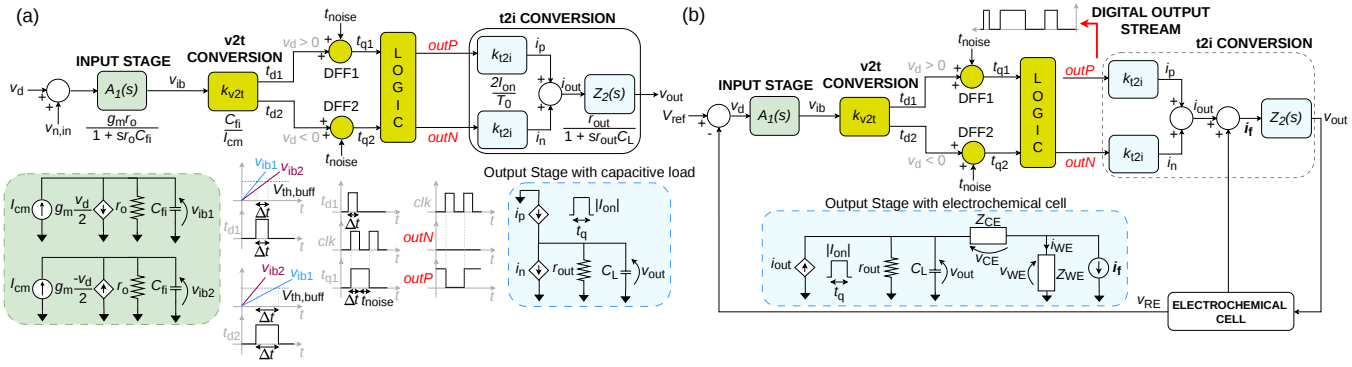

Fig. 4: (a) FI-DIGOTA open loop block diagram (b) DB potentiostat block diagram.

As detailed for the FI-DIGOTA operating principle, the effect of $v_{\rm d}$ determines a change in the slopes $\frac{I_{\rm cm} \pm g_{\rm m} v_{\rm d}/2}{C_{\rm fi}}$ of $v_{\rm ib1}$ and $v_{\rm ib2}$ signals, leading to a time difference (Δt) in the point of time in which these signals cross the threshold voltages of the two digital buffers ($V_{\rm th,buff}$). Thereby, the time difference between the commutations of $v_{\rm d1}$ and $v_{\rm d2}$ signals is directly proportional to Δt and, in the block diagram in Fig. 4a, it is represented by the $t_{\rm d}$ signals that are obtained, from an analytical point of view, multiplying the input stage transfer function times the ratio $C_{\rm fi}/I_{\rm cm}$, where $I_{\rm cm}$ is the common mode current injected in $C_{\rm fi}$ during the states (0,0),(1,1). This mechanism, depicted in Fig. 4a, brings the two digital buffers to perform a voltage-to-time (v2t) conversion.

Unlike in the DIGOTA considered in [34], where the signals which contain the information about $v_{\rm d}$ drive the output stage directly, in the FI-DIGOTA $v_{\rm d1}$ and $v_{\rm d2}$ are sampled by the D-FFs, so that their transitions are synchronized with the nearest clock edge, resulting in the $v_{\rm q}$ signals in which the duration of the time intervals between two transitions of $v_{\rm ib1}$ and $v_{\rm ib2}$, which conveys the information about $v_{\rm d}$, is constrained to be an integer multiple of the clock cycle ($T_{\rm clk}$). The time-domain information is therefore affected by a quantization error, that is described in our model as an additive white noise $t_{\rm noise}$, with uniform amplitude distribution in the (-$T_{\rm clk}$, $T_{\rm clk}$) range, uncorrelated to the input signal, under the same assumptions routinely considered in the analysis of oversampled data converters [36].

As in [34], the output stage, when active, sources (sinks) a nearly constant current $i_{\rm p}$ ($i_{\rm n}$) into the output impedance Z_2 during $t_{\rm q1}$ ($t_{\rm q2}$), thus effectively performing a time-to-current (t2i) conversion and, overall, translating the input differential voltage ($v_{\rm d}$) into a current. Following the same approach in [34] the output stage can be described in the frequency domain as a parallel RC impedance driven by a pulsed current and contributes with a pole to the FI-DIGOTA open-loop gain.

III. DB Potentiostat Operation and Frequency-Domain Analysis

This section describes the operation of the DB potentiostat and derives its frequency-domain model based on the equivalent representation of the electrochemical cell.

A. Electrochemical Cell Model

A standard three-electrode configuration is assumed. The working electrode (WE) is modeled using a Randles equivalent extracted from the characterization of the mesoporous Pt microelectrode described in Sect. IV. The charge-transfer resistance is in parallel with a constant phase element (CPE), as shown in Fig. 2b. The solution resistance, which is in the kΩ range, is neglected because the corresponding voltage drop is negligible for the nA-range currents targeted in this work [37].

Experimental characterization of the microelectrode, discussed in Sect. IV, yields $C_{\rm p}$ = 7 nF and $R_{\rm p}$ = 220 MΩ, consistent with reported values [37], [38]. The counter electrode (CE) impedance is assumed negligible with respect to the WE and is therefore omitted.

B. DB Potentiostat Static and Dynamic Analysis

The proposed DB potentiostat (Fig. 2b) embeds the FI-DIGOTA in a feedback loop with the electrochemical cell for amperometric sensing. The voltage at the reference electrode (RE), $v_{\rm RE} = v^-$, is regulated to $V_{\rm ref} = v^+$ by sourcing or sinking discrete charge packets $i_{\rm p}T_{\rm clk}$ and $i_{\rm n}T_{\rm clk}$ at the CE, where $i_{\rm p}$ and $i_{\rm n}$ are the output-stage currents.

Under static conditions, the average output current equals the faradaic current $i_{\rm f}$, which can be expressed considering the number of active digital pulses (p, n) over an acquisition window of $MT_{\rm clk}$ as

$$i_{\rm f} = \frac{p\, i_{\rm p} - n\, i_{\rm n}}{M}. \tag{1}$$

While (1) has been used in prior work [29], [32], a frequency-domain signal and noise analysis of the DB potentiostat is still lacking and is developed in the following.

C. DB Potentiostat Frequency-Domain Analysis

Based on the small-signal model of the FI-DIGOTA in Fig. 4a and on the Randles equivalent of the electrochemical cell, the frequency-domain behavior of the DB potentiostat can be derived.

Referring to the block diagram in Fig. 4b, the quantized pulse width $t_{\rm q}$ conveys the information associated with the timing difference Δt, while the effect of time quantization is modeled as an additive noise contribution, which is taken into

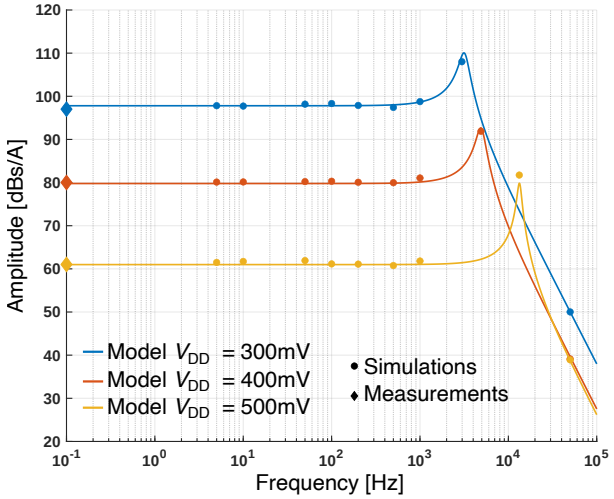

Fig. 5: DB potentiostat signal transfer function with different V_{DD}, comparison between analytical model, simulations and measurements.

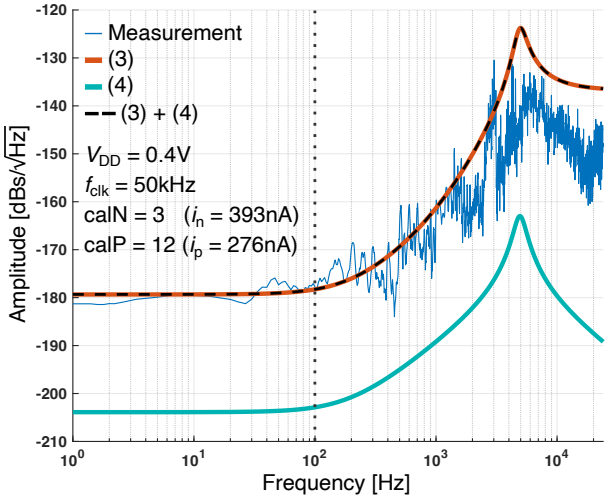

Fig. 6: DB potentiostat noise power spectrum at V_{DD} = 0.4 V, comparison between analytical model and measurement.

account along with the input-referred noise source $v_{\mathrm{n,in}}$ of the potentiostat.

The characterization of the DB potentiostat is carried out by analyzing the variation of t_{q} as a function of the faradaic current i_{f} for the signal transfer function, and by considering the contribution of the quantization noise (t_{noise}) and of the FI-DIGOTA input-referred noise ($v_{\mathrm{n,in}}$) for the noise transfer functions. For simplicity, and consistently with the considered operating conditions ($i_{\mathrm{f}} > 0$), only the pull-up transistor M5 is included in the output-stage model.

1) Signal Transfer Function: From the block diagram in Fig. 4b, the signal transfer function relating the digital pulse width t_{q1} to the faradaic current ($i_{\mathrm{f}} = i_{\mathrm{WE}} = i_{\mathrm{CE}}$) can be expressed as

$$\begin{aligned}\frac{t_{\mathrm{q1}}}{i_{\mathrm{f}}} &= \frac{Z_2(s)A_1(s)k_{\mathrm{v2t}}}{1+A_1(s)k_{\mathrm{v2t}}k_{\mathrm{t2i}}Z_2(s)} \\ &= \frac{g_{\mathrm{m}}r_{\mathrm{o}}\frac{C_{\mathrm{fi}}}{I_{\mathrm{cm}}}r_{\mathrm{out}}}{(1+sr_{\mathrm{o}}C_{\mathrm{fi}})(1+sr_{\mathrm{out}}C_{\mathrm{L}})+2g_{\mathrm{m}}r_{\mathrm{o}}\frac{C_{\mathrm{fi}}}{I_{\mathrm{cm}}}r_{\mathrm{out}}\frac{I_{\mathrm{on}}}{T_0}}.\end{aligned} \tag{2}$$

The DB potentiostat can be modeled as a second-order system. The low-frequency gain is determined by the intrinsic gain of the input stage, the ratio $C_{\mathrm{fi}}/I_{\mathrm{cm}}$, and the output resistance r_{out}, while the pole frequencies are set by the time constants $r_{\mathrm{o}}C_{\mathrm{fi}}$ and $r_{\mathrm{out}}C_{\mathrm{L}}$, where the output capacitance value C_{L} has been kept equal to C_{P} = 7 nF.

Fig. 5 shows the comparison of the model described in (2) with transistor-level transient simulations and measurements at different V_{DD} while maintaining a fixed clock frequency of 50 kHz. The parameters used to evaluate (2) are reported in Table I for V_{DD} = 0.4 V. The frequency behavior of t_{q1} is obtained from the FFT of the normalized v_{outP} signal. Since the DB potentiostat operates in chronoamperometric mode, the measured v_{outP} spectrum reflects the DC response of (2).

As V_{DD} decreases, the DC gain increases, resulting in higher sensitivity of the digital output to variations of the faradaic current. In the subthreshold regime, this behavior arises from the exponential dependence of the average output current I_{on}, to which the transfer function is inversely related. The gain peaking observed near the corner frequency is predicted by the second-order signal transfer function, whose poles are set by the FI-DIGOTA and electrochemical-cell time constants. Since the second pole is only weakly dependent on V_{DD}, the overall gain-bandwidth product slightly improves at lower supply voltages. Fig. 5 shows good agreement between model, simulations and low-frequency chronoamperometric measurements.

TABLE I: FI-DIGOTA Simulations Parameters (V_{DD} = 0.4 V)

Parameter	Unit	Value
T_0	μs	103
g_{m}	nS	61
r_0	GΩ	89
r_{out}	kΩ	102
C_{fi}	fF	1.9
I_{on}	nA	8.1
I_{cm}	pA	0.8

2) Noise Transfer Function: Considering Fig. 4b, the noise transfer function (NTF) relating the quantization noise introduced by the D-FFs and the digital output t_{q1} can be expressed as:

$$\begin{aligned}\frac{t_{\mathrm{q1}}}{t_{\mathrm{noise}}} &= \frac{k_{\mathrm{t2i}}Z_2(s)A_1(s)k_{\mathrm{v2t}}}{1+A_1(s)k_{\mathrm{v2t}}k_{\mathrm{t2i}}Z_2(s)} \\ &= \frac{(1+sr_{\mathrm{o}}C_{\mathrm{fi}})(1+sr_{\mathrm{out}}C_{\mathrm{L}})}{(1+sr_{\mathrm{o}}C_{\mathrm{fi}})(1+sr_{\mathrm{out}}C_{\mathrm{L}})+2g_{\mathrm{m}}r_{\mathrm{o}}\frac{C_{\mathrm{fi}}}{I_{\mathrm{cm}}}r_{\mathrm{out}}\frac{I_{\mathrm{on}}}{T_0}}\end{aligned} \tag{3}$$

The transfer function in (3) reveals second-order noise shaping, which effectively attenuates the quantization noise related to the D-FFs by the FI-DIGOTA DC gain, i.e. $A_0 \simeq 2g_{\mathrm{m}}r_{\mathrm{o}}\frac{C_{\mathrm{fi}}}{I_{\mathrm{cm}}}r_{\mathrm{out}}\frac{I_{\mathrm{on}}}{T_0}$.

On the other hand, the NTF from the FI-DIGOTA equivalent

input noise source $v_{\mathrm{n,in}}$ to t_{q1} can be expressed as:

$$\frac{t_{\mathrm{q1}}}{v_{\mathrm{n,in}}} = \frac{A_1(s)k_{\mathrm{v2t}}}{1+A_1(s)k_{\mathrm{v2t}}k_{\mathrm{t2i}}Z_2(s)} = \frac{(1+sr_{\mathrm{out}}C_{\mathrm{L}})g_{\mathrm{m}}r_{\mathrm{o}}\frac{C_{\mathrm{fi}}}{I_{\mathrm{cm}}}}{(1+sr_{\mathrm{o}}C_{\mathrm{fi}})(1+sr_{\mathrm{out}}C_{\mathrm{L}})+2g_{\mathrm{m}}r_{\mathrm{o}}\frac{C_{\mathrm{fi}}}{I_{\mathrm{cm}}}r_{\mathrm{out}}\frac{I_{\mathrm{on}}}{T_0}} \quad (4)$$

Remarkably, (4) reveals first-order shaping of the FI-DIGOTA input noise, and a low-frequency noise attenuation of $T_0/(2r_{\mathrm{out}}I_{\mathrm{on}})$.

D. Noise Sources

In the proposed model, the quantization noise t_{noise} has been modeled as a discrete-time random process with a uniform amplitude distribution between $-T_{\mathrm{clk}}$ and T_{clk}, i.e. with a variance $T_{\mathrm{clk}}^2/3$ corresponding to the total noise power, and with a white power spectral density (PSD). It is important to note that, considering the FI-DIGOTA operation described above and illustrated in the waveforms of v_{cmp}, v_{outP} and v_{outN} in Fig. 3, the digital signals $outP$, $outN$ are inherently sampled at the FI-DIGOTA self-oscillation frequency $f_0 = 1/T_0$, which is significantly lower than the clock frequency. As a consequence, each noise sample is spaced in time by T_0 and thus, under the white noise assumption, the quantization noise power is evenly spread from DC to the Nyquist frequency $f_0/2$ and its PSD $S_{\mathrm{t_{noise}}}$ can be estimated as:

$$\int_{-f_0/2}^{f_0/2} S_{\mathrm{t_{noise}}}(f)\,df = \frac{T_{\mathrm{clk}}^2}{3} \rightarrow S_{\mathrm{t_{noise}}}(f) = \frac{T_{\mathrm{clk}}^2 T_0}{3} \quad (5)$$

On the other hand, in analogy with [34], the FI-DIGOTA equivalent input noise is dominated by the shot noise contribution of the devices of the FI input stage, whose PSD can be expressed as:

$$S_{\mathrm{v_n,in}}(f) = \frac{2qI_{\mathrm{cm}}}{g_{\mathrm{m}}^2} \quad (6)$$

where q is the elementary charge. Remarkably, the flicker noise contribution of the FI input stage is completely suppressed thanks to the dynamic operation of the FI input stage [39], resulting in competitive noise performance in the target biosensing application without requiring area- and power-hungry chopping or auto-zeroing techniques.

E. Overall Noise and Noise Model Validation

Fig. 6 shows the overall noise spectrum referred to t_{q1} together with the individual quantization- and shot-noise contributions. These spectra are obtained from the NTFs in (3) and (4) and the source PSDs in (5) and (6), respectively, for $V_{\mathrm{DD}} = 0.4\,\mathrm{V}$. The figure reveals that the quantization noise is dominant, and the behavior over frequency is characterized by +40 dB/dec and +20 dB/dec slopes, and a flat noise floor at low frequency.

In the same figure, the noise spectra calculated by the model are compared to the digital output noise power spectrum measured for the fabricated potentiostat at V_{DD} = 0.4 V with reference to the test setup described in Sect.V under zero input signal. The reported measurement was obtained by averaging five records according to Welch's periodogram method, using a Blackman window, a sampling frequency of 50 kHz and an acquisition time of 5 s.

The calculated and measured noise spectra are in reasonably good agreement at low frequency and up to the Nyquist frequency related to the inherent sampling at the FI-DIGOTA self-oscillation frequency, in which the hypotheses of the average DIGOTA model in [34] are clearly no longer valid, and a peak is observed. Finally, the measured noise spectrum reveals no $1/f$ component at low frequency, confirming the inherent flicker noise suppression of the proposed DB-potentiostat.

When required, the noise expressed in terms of t_{q1} can be converted into a current-equivalent contribution using the same time-to-current gain k_{t2i} introduced in the FI-DIGOTA model. Accordingly, rms noise amplitudes are multiplied by k_{t2i}, whereas power spectral densities are multiplied by k_{t2i}^2.

IV. Mesoporous Pt Microelectrode and Electrochemical Readout Co-Design

As a crucial element for enabling non-enzymatic glucose detection at nanowatt-level power, the mesoporous Pt microelectrodes and their co-design with the electronic readout are detailed in this section. First, the choice of microelectrodes and mesoporous Pt nanostructuring is justified, followed by the description of the fabrication process. The microelectrode current–concentration relation is then introduced to estimate the expected faradaic current and, finally, to define the corresponding DB potentiostat design parameters.

A. Microelectrode Design Rationale

Non-enzymatic glucose detection on Pt has been investigated since the early studies on bare platinum electrodes [40], [41], and nanostructured electrodes have since been widely explored to increase the electroactive area and improve the glucose response [42], [43]. Here, mesoporous Pt nanostructuring is exploited as a co-design lever: it increases the electroactive surface while keeping the absolute faradaic current in the range required by an ULV/ULP DB potentiostat, enabling nA-range direct digitization within a sub-300 mV electrochemical operating window.

The rationale for this choice follows from the different role played by accessible roughness in diffusion-controlled and kinetically controlled reactions. When the diffusion length established during the potential step exceeds the characteristic scale of the mesoporous features, fast electron-transfer reactions under diffusion control are governed mainly by mass transport to the microelectrode, and their limiting current scales primarily with geometrical area [44], [45]. Conversely, for kinetically controlled reactions, the faradaic current depends strongly on the accessible nanostructured surface and scales with the rough electroactive area. A larger accessible roughness factor can therefore increase the faradaic current attainable for slow surface-controlled reactions.

This distinction is particularly relevant for glucose oxidation on Pt, which is limited by surface kinetics and by the availability of active catalytic sites [40], [41]. On smooth Pt electrodes, the glucose-oxidation current at low overpotential is generally limited by sluggish surface kinetics and by the

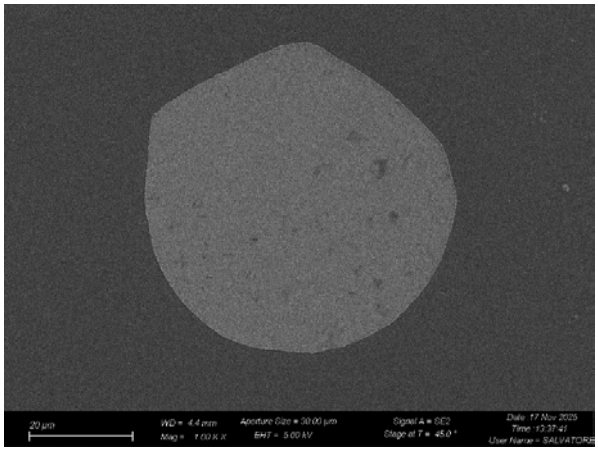

(a)

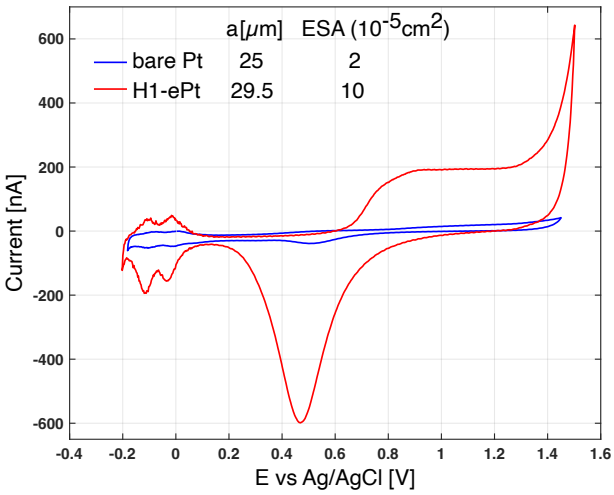

(b)

Fig. 7: microelectrode characterization: (a) scanning electron micrograph of the microdisc embedded in glass with H1-ePt performed by a ZEISS Supra 40 and merlin field emission scanning electron microscope (FESEM), (b) cyclic voltammetry (CV) in acid with and without H1-ePt

restricted number of active sites. The mesoporous Pt film increases the electroactive area required to enhance the low-overpotential glucose-related response, consistently with the large electrochemical-to-geometrical area ratio reported for mesoporous Pt electrodes [46], while the microdisc geometry prevents this increase from translating into an excessive absolute current. In this sense, miniaturization is used primarily as a current-scaling tool, so that the electrode response remains compatible with direct current digitization at $V_{\mathrm{DD}} = 0.3\,\mathrm{V}$ and nanowatt-level power.

Accordingly, Sect. VI validates the current readout using ferrocyanide oxidation as a standard diffusion-controlled redox probe, while Sect. VII addresses the target kinetically controlled glucose-oxidation reaction, including ascorbic acid as a representative interferent in the proof-of-concept validation.

B. Current–Concentration Relation for Microdisc Electrodes

Microelectrodes are generally used to measure electron-transfer rates of fast reactions [44], and microdisc-shaped electrodes exhibit stable spherical diffusion under quiescent conditions [45]. When embedded within an insulating material of sufficiently large radial dimensions, microdiscs can achieve steady-state limiting currents under mass-transport-controlled conditions, described by

$$i_{\mathrm{L}} = 4nFDca \tag{7}$$

where n, F, D, c, and a denote the number of transferred electrons, the Faraday constant, the diffusion coefficient, the bulk analyte concentration, and the electrode radius, respectively. Once the electrode geometry and reaction mechanism are defined, the bulk analyte concentration can be estimated from the limiting current (i_{L}) over a time scale ranging from sub-second to a few seconds, depending on factors such as temperature, solution viscosity, and electrode radius.

In this work, this relation is used as the diffusion-controlled current-scaling reference for the ferrocyanide/ferricyanide validation experiments reported in Sect. VI.

C. Fabrication and Characterization of the Mesoporous Pt Film

Mesoporous Pt microdisc electrodes were fabricated according to the method first reported by Attard et al. [35], later used as hydrogen-peroxide sensors by Evans et al. [46] and by the authors in previous studies on dissolved oxygen and pH detection [47].

The microelectrodes were fabricated starting from platinum microdisc electrodes by Metrohm with nominal radii of 5 µm, 25 µm, 50 µm, and 100 µm. The electrodes were polished with multigrade silicon carbide (SiC) papers, diamond powder (1 µm), and alumina powder (0.03 µm) until mirror finishing. The real geometrical area was measured from field emission scanning electron microscope (FESEM) micrographs. Electrochemical cleaning was carried out in 0.5 M H_2SO_4 between -0.45 V and +1.00 V vs. silver/silver chloride (Ag/AgCl) until reproducible cyclic voltammograms were obtained. This cleaning was performed before each experiment.

The mesoporous Pt film was electrodeposited from a hexagonal (H1) liquid-crystalline phase composed of the non-ionic surfactant Brij 58 (0.42 g), hydrogen hexachloroplatinate hydrate (0.29 g), distilled water (0.29 g), and two drops of heptane [48], at a potential of -0.06 V vs. Ag/AgCl until a charge density of 4 µC/cm^2 was passed. The geometrical area, shown in Fig. 7a, was evaluated from FESEM micrographs and from the limiting current according to (7). The roughness factor was evaluated from the cyclic voltammograms recorded during electrochemical cleaning after electrodeposition, by measuring the areas under the hydrogen adsorption/desorption peaks and using a conversion factor of 210 µC cm^{-2} to determine the active surface, according to Trasatti's method [49] and corrected following Biegler's observation [50]. The cyclic voltammetry in acid with and without H1-ePt nanostructuration are shown in Fig 7b.

Based on the developed model, the DB potentiostat is expected to track the faradaic current determined by the electrode impedance and reaction kinetics. The measurements in Sect.VI and Sect.VII validate this behavior using both diffusion-controlled and kinetically-controlled electrochemical processes.

D. Digital-Based Potentiostat Co-Design

The FI-DIGOTA was designed and fabricated in 130 nm CMOS technology to operate from a 0.3 V supply, reducing readout power while exploiting the energy-efficiency advantage of digital and digital-based analog circuits in the near-threshold regime [34], [51].

The floating-inverter input stage is sized to include the electrochemical reference potential within its input common-mode range, while taking into account the input-device noise contribution predicted by the analysis of Sect. III. The output stage is implemented as a programmable pull-down/pull-up network controlled by two 8-bit calibration words, calN and calP, which set the effective sink and source currents, i_{n} and i_{p}, respectively. This programmability provides the flexibility required to cover different electrode sizes, analytes and supply voltages. For each condition, calN and calP are selected according to the required current range and saturation margin, using the electrode scaling in (7) where applicable, while also considering their impact on the faradaic current quantization noise. The remaining non-critical digital gates use minimum-strength standard cells to reduce switching energy.

The clock frequency defines the time resolution of the unit current pulses, while the acquisition time (T_{acq}) sets the effective bandwidth of the averaged current estimate. Since the target electrochemical measurements do not impose a stringent bandwidth requirement, f_{clk} and T_{acq} are selected to favor energy-efficient conversion and quantization-noise averaging rather than high-speed operation. In this prototype, $f_{\mathrm{clk}} = 50\,\mathrm{kHz}$ and $T_{\mathrm{acq}} = 5\,\mathrm{s}$ are kept fixed throughout the electrochemical measurements, providing common timing and bandwidth conditions across different electrodes, analytes and calibration settings.

The layout and micrograph of the fabricated FI-DIGOTA are shown in Fig. 8. The circuit occupies 11,532 $\mu\mathrm{m}^2$, with more than 90% allocated to the programmable output stage. This area overhead is the cost of prototype calibration flexibility; in a glucose-dedicated implementation, the output-stage strength could be fixed, reducing the associated area.

V. Digital Potentiostat Electrical Characterization

Before validating the DB potentiostat as an electrochemical sensing platform, the FI-DIGOTA readout was characterized at circuit level through post-layout simulations under PVT variations and multidie measurements, in order to assess the robustness of the current-to-digital conversion at the target 0.3 V supply.

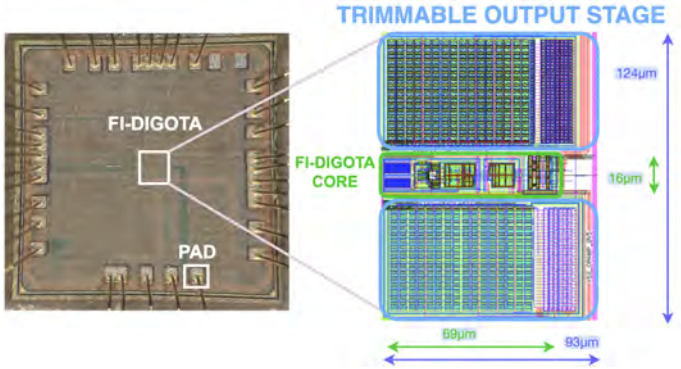

Fig. 8: FI-DIGOTA micrograph and layout.

TABLE II: Performance comparison with respect to temperature and process variations

T [°C]	Process	Sensitivity [LSB/nA]	Linearity [R^2]	Max. error [a] [LSB]	Rel. error [b] [%]
27	TYP	22261	0.998	2112	-
	SS	14220	0.991	3897	-36.12
	SF	18677	0.997	3555	-16.10
	FS	24961	0.997	3806	12.13
	FF	28834	0.995	5266	29.53
20	TYP	27326	0.998	3828	22.75
27		22261	0.998	2112	-
35		21401	0.998	2859	-3.86
50		15503	0.995	3412	-30.36

[a] compared to nominal fit,
[b]percentage of slope variation compared to the typical case (TYP, 27°C).

A. Post-Layout Simulations under PVT Variations

The FI-DIGOTA current-readout capability was first evaluated by post-layout simulations at $V_{\mathrm{DD}} = 0.3\,\mathrm{V}$, where the circuit is most sensitive to process and temperature variations.

The simulation setup reproduces the DB-potentiostat configuration in Fig. 2b, using the equivalent electrochemical-cell model discussed in Sec. III-A, with $C_{\mathrm{p}} = 7\,\mathrm{nF}$ and $R_{\mathrm{p}} = 220\,\mathrm{M\Omega}$, and ideal current sources to emulate the faradaic current. The FI-DIGOTA parameters are those used in the non-enzymatic glucose measurements of Sec. VII: $f_{\mathrm{clk}} = 50\,\mathrm{kHz}$, calN = 1 ($i_{\mathrm{n}}$=10.16 nA), calP = 3 ($i_{\mathrm{p}}$=4.89 nA), and $T_{\mathrm{acq}} = 5\,\mathrm{s}$.

Post-layout simulations under temperature variations, in a range compatible with wearable applications and in the typical process corner, are shown in Fig. 9, while simulations under process-corner variations at fixed temperature are reported in Fig. 10. The simulations are compared with the glucose measurements reported in Sec. VII, showing good agreement. Temperature and process-corner variations mainly affect the slope of the current-to-digital characteristic and, to a lesser extent, its linearity. These variations can be compensated by exploiting the tunable output stage, as demonstrated in [52]. Monte Carlo simulations under process and mismatch variations yield a standard deviation of the DB-potentiostat sensitivity of $\sigma = 21325.53\,\mathrm{LSB}$, as shown in Fig. 11. Finally, Table II summarizes the main parameters as process corner and temperature vary, including, for each case, the maximum error with respect to the nominal fit and the relative slope variation with respect to the typical condition (TYP corner, $T = 27\,^{\circ}\mathrm{C}$).

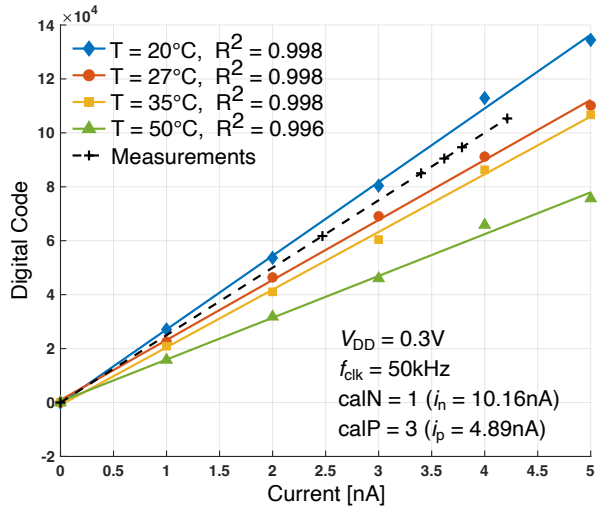

Fig. 9: Calibration curve against temperature variations at V_{DD} = 0.3 V and f_{clk} = 50 kHz.

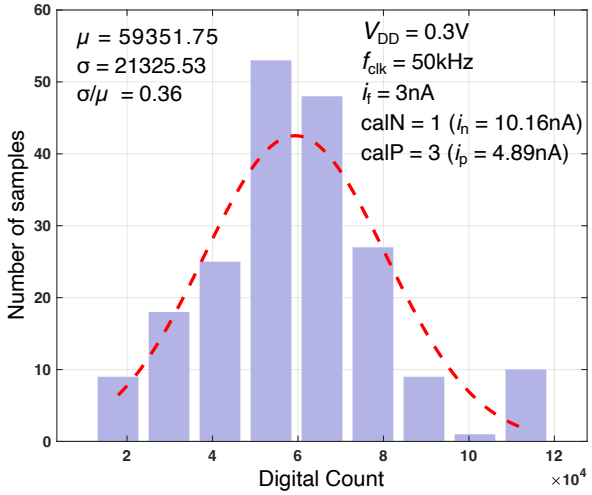

Fig. 11: Mismatch current readout variations with i_{f} = 3 nA at V_{DD} = 0.3 V and f_{clk} = 50 kHz.

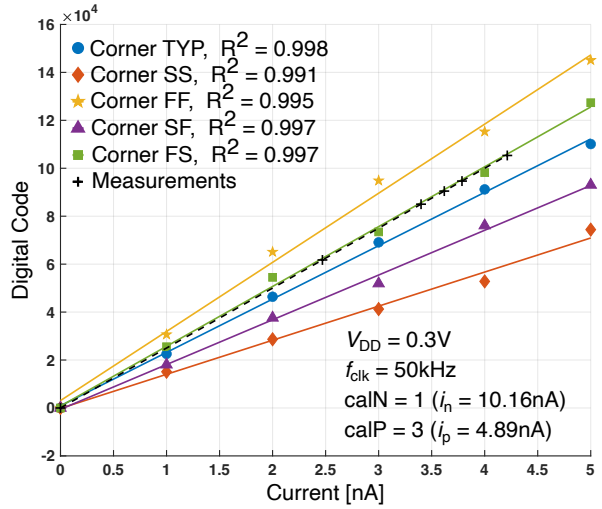

Fig. 10: Calibration curve against process variations at V_{DD} = 0.3 V and f_{clk} = 50 kHz.

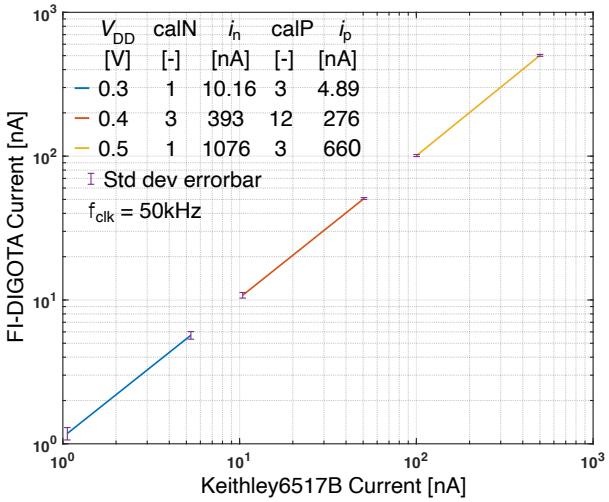

Fig. 12: Multi-dice FI-DIGOTA current readout characterization with resistive load across 5 dice.

B. Multidie Measurements

To test the operation of the fabricated FI-DIGOTA as a current readout under process variations, five dice were measured using a discrete-component RC load. A regulated DC power supply was connected in series with the load to tune the desired output current, i_{out}. The measurements were carried out at different V_{DD} values by externally varying the FI-DIGOTA output current over more than two orders of magnitude and estimating the current from the digital output using (1).

The obtained results are shown in Fig. 12 and summarized in Table III, demonstrating consistent current readout across five dice. In detail, the average standard deviation across five dice of the readout current, normalized to the current read with the picoamperometer, is approximately 4.5 %, in line with the requirements of PoC diagnostics.

VI. ULV ULP Electrochemical Sensing Platform

This section describes the experimental setup used for the electrical and electrochemical measurements and validates the DB potentiostat readout in a diffusion-controlled regime using ferrocyanide oxidation as a standard redox-probe reaction.

A. Experimental Test Setup

The electrical measurements were performed using a Keithley 6517B source meter, an Agilent 34401A multimeter, an Agilent 33250A signal generator, a Rigol DP832A DC power supply and a Rigol MSO5104 oscilloscope. Two Keithley 6517B source meters were used to monitor the electrochemical and supply currents, while the digital pulses ($outP$,$outN$) were recorded with the oscilloscope and processed in MATLAB to evaluate the faradaic current by (1).

TABLE III: FI-DIGOTA Current Readout Multidie Characterization Across Five Dice

V_{DD} [V]	Mean [nA]	σ [nA]	Min [nA]	Max [nA]
0.3	1.18	0.12	1.08	1.37
	5.68	0.35	5.25	6.21
0.4	10.79	0.48	10.12	11.36
	50.77	0.76	49.67	51.58
0.5	100.99	1.64	98.23	102.41
	502.28	7.75	490.14	511.47

The same setup was also used to obtain the experimental results supporting the frequency-domain signal and noise analysis of the DB potentiostat presented in Sec. III, while the standalone characterization of the FI-DIGOTA as an amplifier is reported in [31].

All electrochemical experiments were performed inside a grounded Faraday cage. Control experiments and electrode characterization were carried out using a Metrohm PGSTAT204 potentiostat/galvanostat controlled by Nova 2.0. Depending on the cell design, either an Ag/AgCl saturated-sodium chloride (NaCl) RE or a Pt-coil pseudo-reference immersed in the testing solution was used. A platinum bar was used as CE, and the microdisc electrodes described in Sect. IV were used as WE.

B. Amperometric Detection in a Diffusion-Controlled Regime: Ferrocyanide Sensing

Ferrocyanide oxidation was used as a standard diffusion-controlled redox reaction to validate the current-readout capability of the DB potentiostat under well-defined electrochemical conditions. The microelectrode was first characterized by commercial instrumentation and then interfaced with the DB potentiostat to measure the oxidation current.

1) Electrode Characterization: Chronoamperograms were first acquired with the PGSTAT204 to estimate the time required to reach the steady-state current. The same potential step was then applied with the DB potentiostat. The reaction current was acquired for 5 s, averaged according to (1), and compared with that measured with the PGSTAT204 over the same interval.

As shown in Fig. 13 the Linear Sweep Voltammetry (LSV) of a microdisc electrode recorded in ferrocyanide solution using both mesoporous and bare Pt electrodes displayed very similar electrochemical behavior. In fact, they showed comparable electrochemical reversibility (both with a slope of -24 mV) and limiting current normalized by geometric area. These similarities in diffusion-controlled behavior between the mesoporous and bare Pt electrodes are consistent with previous findings [53].

The steady-state current response of Pt microdisc electrodes in sodium ferrocyanide ($Na_4Fe(CN)_6$) was used to evaluate the operating range of the DB potentiostat across three orders of magnitude, from hundreds of pA to hundreds of nA. To span the desired current range, three electrodes with different radii and several $Na_4Fe(CN)_6$ concentrations in 0.5 M NaCl were employed. The characterization of the three sensors is reported in Fig. 14a. When the current is normalized to the respective limiting current i_L, a potential shift due to kinetic limitations

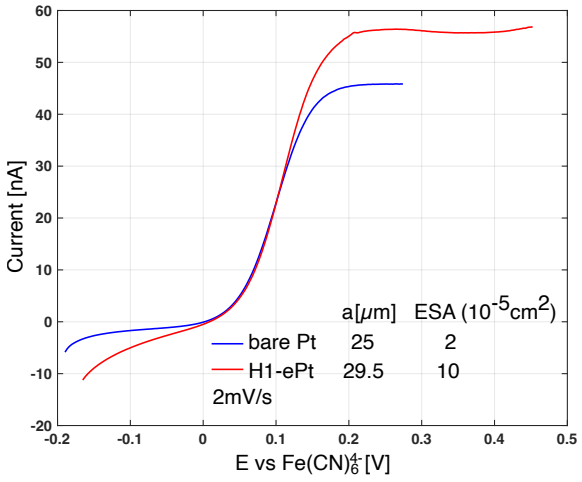

Fig. 13: Ferrocyanide ($Fe(CN)_6^{4-}$) linear sweep voltammetry (LSV) at 2 mV/s scan rate with and without H1-ePt

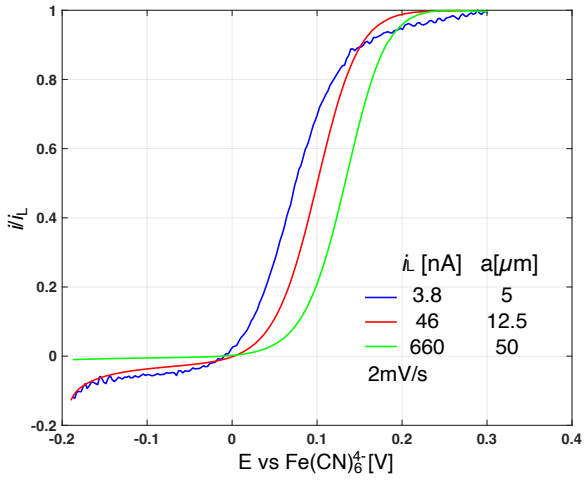

(a)

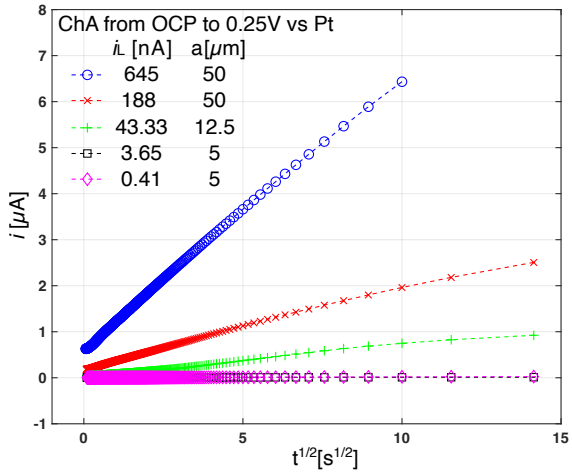

(b)

Fig. 14: Electrode characterization for ferrocyanide sensing: (a) linear sweep voltammetry (LSV) at 2 mV/s scan rate acquired on micro-discs with different radius, (b) Chronoamperograms from open circuit potential (OCP) to 0.25 V vs Pt and fit according to Mahon-Oldham. As the current decreases, the measurements refer to a $Na_4Fe(CN)_6$ concentration equal to: 50 mM, 15 mM, 15 mM, 3 mM, 0.3 mM.

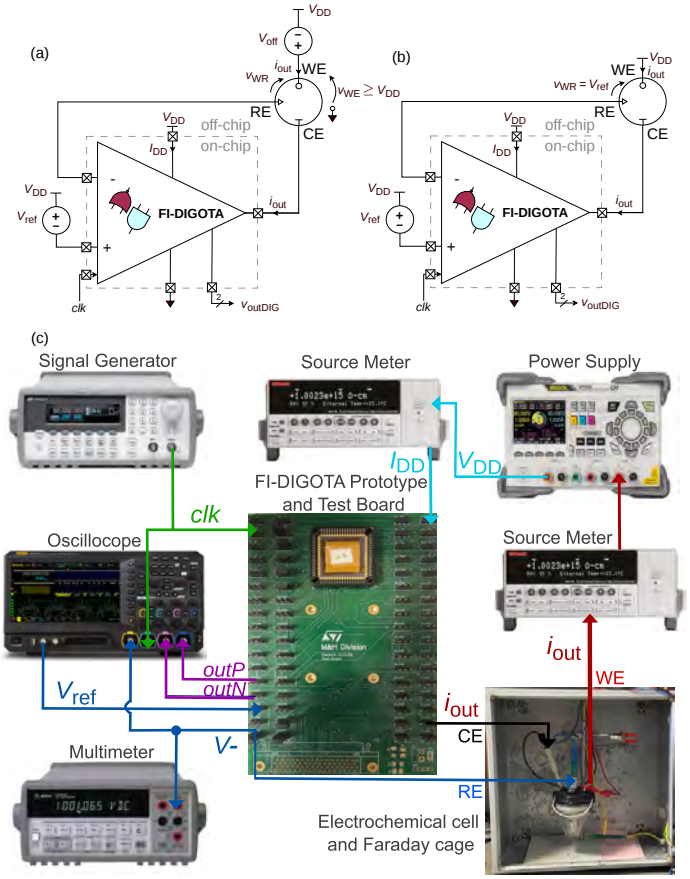

Fig. 15: Measurement setup: (a) ferrocyanide sensing; (b) non-enzymatic glucose sensing; (c) block diagram.

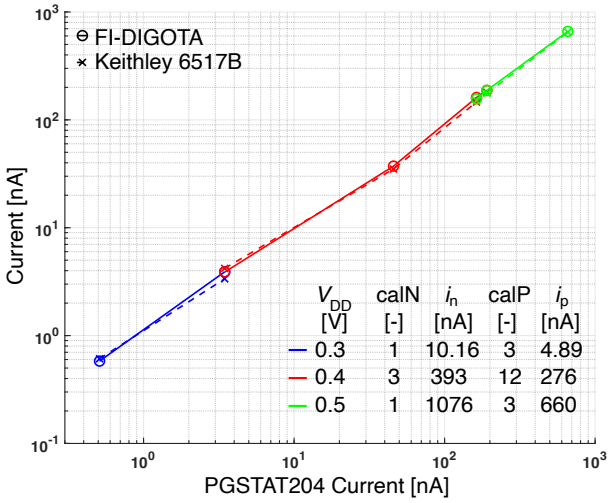

Fig. 16: DB potentiostat ferrocyanide characteristic.

becomes evident: the smaller the electrode radius, the more negative the overpotential and the half-wave potential. The measurements in Fig. 14a were performed using different microdisc electrodes and analyte concentrations in order to span the target current range; electrode-to-electrode dispersion is therefore included in the experimental validation but is not separately isolated in this proof-of-concept study.

Chronoamperometry experiments were performed in several solutions of different concentration of $Na_4Fe(CN)_6$ by a potential step from open circuit potential (OCP) to +250 mV vs OCP for 120 s in accordance with the voltammetries in Fig. 14a. Fig. 14b shows such current transients obtained and compared with the fittings to the Mahon-Oldham equation (dashed lines) [54]. For all the electrode radii, the fittings agree at long times, indicating that the electrodes follow the expected behavior of a microdisc. At short times, data are not perfectly in line with the theoretical curves probably due to some adsorbed oxygen on the Pt electrode because the solution was not degassed. The current transients after the potential step from OCP to +250 mV were acquired using the PGSTAT204, the FI-DIGOTA, and the Keithley 6517B.

2) DB Potentiostat Measurements: The same ferrocyanide sensing measurements have also been performed using the DB potentiostat at three supply voltages (300 mV, 400 mV and 500 mV) with a fixed 50 kHz f_{clk} and with output-stage calibrations selected according to the expected current range and indicated in Fig. 16. The measurement setup for ferrocyanide sensing is shown in Fig. 15a. As reported in [31], the FI-DIGOTA input common-mode range is 170–230 mV, 180–300 mV and 190–400 mV for V_{DD} = 0.3 V, 0.4 V and 0.5 V, respectively. Ferrocyanide oxidation requires a voltage between WE and RE ($v_{WR} = v_{WE} - v_{RE}$) of 0.25 V. While this condition can be directly accommodated at $V_{DD} = 0.4$ V and 0.5 V, at $V_{DD} = 0.3$ V it would leave insufficient input common-mode headroom to keep both electrode potentials within the circuit supply rails. Therefore, an external offset was added to the WE potential, resulting in a v_{WE} higher than V_{DD} while preserving the required v_{WR} across the electrochemical cell. The current measured after 100 s from the potential step was acquired by the three systems for 5 s and the comparative data are reported in Fig. 16, revealing that DB potentiostat and commercial instruments (Keithley6517B, PGSTAT204) have identical current responses over more than three decades of current from hundreds of pA to hundreds of nA.

In Fig. 17a, the linear regression of the DB-potentiostat current measurements at $V_{DD} = 400$ mV, obtained from the pulse counts according to (1) at different concentrations, exhibits a linearity of $R^2 = 0.991$. Fig. 17b reports the corresponding digital pulse counts n and p in (1) as a function of the analyte concentration, providing insight into the circuit operation and into the pulse-counting-based current estimate.

The input referred noise has been evaluated with different V_{DD}, averaging the digital output streams for the entire acquisition period. The obtained values are equal to 5.6 pA_{rms}, 46.72 pA_{rms} and 347.03 pA_{rms} for V_{DD} = 0.3 V, 0.4 V, 0.5 V, respectively. Considering equation (7), micro-electrodes do not introduce any detection boundaries and, therefore, the detection limit of the overall system can be evaluated as three times the digital potentiostat input-referred current noise, yielding a value of 16.80 pA at a supply voltage of 0.3 V.

Based on the input referred noise evaluation, the dynamic ranges are evaluated as function of V_{DD} and considering the current range measured in Fig. 16, giving back values of 59.68 dB, 71.72 dB, 65.45 dB for V_{DD} equal to 300 mV,

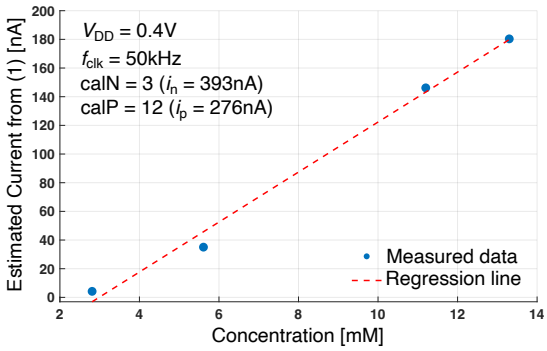

(a)

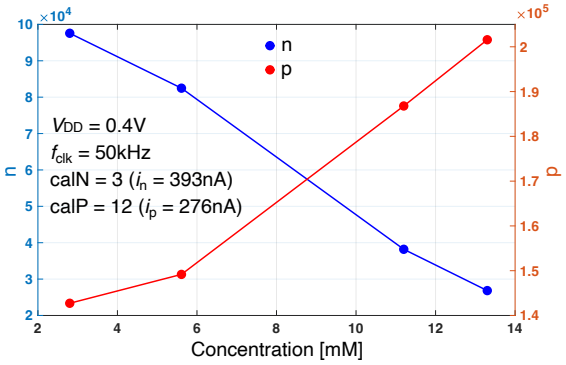

(b)

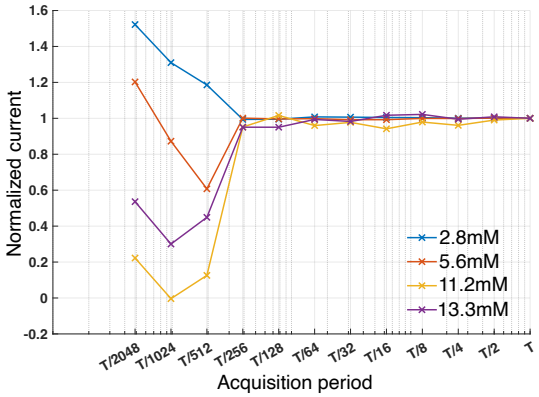

(c)

Fig. 17: DB potentiostat electrical behavior during ferrocyanide oxidation measurements at $V_{DD} = 0.4$ V: (a) calibration curve; (b) digital pulse evolution; (c) normalized current estimate versus acquisition period.

400 mV and 500 mV, respectively. Notably, the dynamic range remains above 59 dB for all tested supply settings, with the programmable output stage allowing the current range to be adapted to the target electrochemical condition.

Finally, Fig. 17c defines the minimum acquisition time, showing the reaction current normalized with respect to its steady-state value, whose estimate is obtained by considering a limited set of samples acquired by the DB potentiostat over $T = 5$s, as well as by considering the full set of acquired data. From the figure, an acquisition time of $T/256$=20 ms is sufficient to obtain a good estimate of the faradaic current.

TABLE IV: FI-DIGOTA and Micro-Electrode parameters for non-enzymatic glucose sensing

Component	Parameter	Unit	Value
FI-DIGOTA	V_{DD}	V	0.3
	f_{clk}	kHz	50
	calN (i_n)	- (nA)	1 (10.16)
	calP (i_p)	- (nA)	3 (4.89)
	Power	nW	1.65
	Sensitivity	LSB/nA	24698
	Current Range	nA	2.27 - 4.21
Electrode	Radius	μm	25
	Nanostructuration	-	H1ePt
	Concentration Range	mM	2-50

This is consistent with the noise analysis presented in Sect.III and with the results in Fig. 6.

VII. Non-Enzymatic Glucose Detection Proof of Concept

In this section the measurement results for the DB potentiostat experimental characterization in the target non-enzymatic glucose monitoring application, which involves the glucose oxidation under a kinetically-controlled regime, are shown.

A. Amperometric detection in a kinetically-controlled regime: the glucose sensing

Here, the characterization of the nanostructured microelectrode for non-enzymatic glucose detection is shown and, subsequently, the measurement results obtained with the DB potentiostat are presented.

1) Electrode Characterization: In practical PoC applications, solution degassing is typically impractical due to its power and time requirements. Therefore, no degassing is performed in this work, and its effects are explicitly considered.

In cyclic voltammetry measurements using bare Pt electrodes of 25 µm of radius, reactions of 20 mM of glucose in aerated 0.1 M phosphate buffer solution (PBS) were not visible at all. With the corresponding H1-ePt nanostructure, the voltammetry changes completely and several peaks associated to electrochemical oxidation reactions appear, as seen in Fig. 18a. The electrochemical oxidation of glucose (GOR) on platinum in neutral phosphate buffer proceeds primarily through dehydrogenation at the C1 carbon.

Among the anomeric forms of glucose, the α-glucose employed in this study it the one that exhibits the lowest reactivity, whereas β-glucose is the most reactive, likely due to the orientation of the anomeric C–H bond. The overall oxidation process is typically described within three distinct potential regions. First (region (1)), the "hydrogen region" (from 0 to 350 mV vs. reversible hydrogen electrode (RHE)), in which the platinum uniquely enables a characteristic oxidative response not observed for other electrode materials or for related organic substrates such as alcohols, aldehydes, or acids. Here, glucose oxidation is strongly influenced by the adsorbed hydrogen, and the hemiacetal moiety serves as the principal reactive site.

Surface-adsorbed glucose or its intermediates govern the reaction pathway. Secondarily (region (2)), the "double-layer region" (from 400 mV to 800 mV vs. RHE) exhibits two oxidation peaks at low scan rates. The peak currents diminish

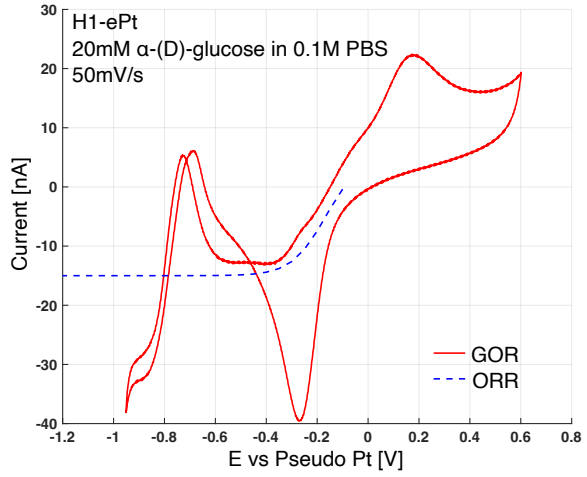

(a)

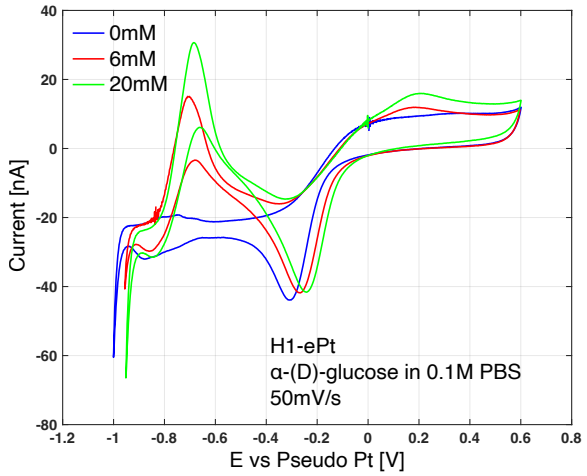

(b)

Fig. 18: Setup for electrochemical current sensing: (a) cyclic voltammetry (CV) with H1ePt nanostructure, (b) cyclic voltammetry (CV) in 0.1 M PBS with different glucose concentrations.

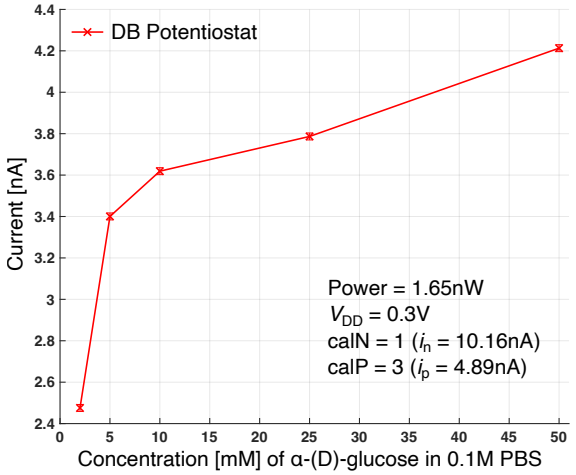

Fig. 19: DB potentiostat calibration curve for non-enzymatic glucose detection.

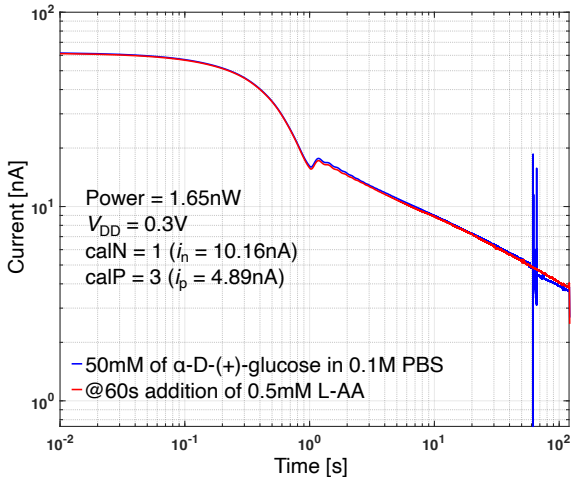

Fig. 20: Current vs time curves responses of H1-ePt to 50 mM of glucose steady (red) and (blue) during the addition at the time 60 s of 0.5 mM of ascorbic acid (L-AA). The spikes in the current correspond to the addition of the interfering solution to achieve a whole concentration of 0.5 mM of L-AA in 50 mM of α-D(+)-glucose in 0.1 M PBS aerated.

as anions or organic specie, in particular glucono-δ-lactone, adsorb onto the surface and it depends on glucose concentration.

In the region (1) and (2) the presence of oxygen dissolved in the solution generates an additional reaction, the oxygen reduction reaction (ORR) that compete with the GOR generating a sum of the two current contributions. The only one region in which there is a peak attributed to the complex reaction mechanism of the oxidation of glucose and that has no additional current dependent on mass transport of other species naturally present in the solution is (3), the "oxide region" ($>$ 900 mV vs. RHE) in which the glucose reacts with platinum oxide, and lactone-type poisoning products undergo further oxidative decomposition.

Therefore, among all the peaks promoted by the oxidation of glucose, the only one which does not compete with the ORR happens in the H1-ePt during the first stages of the platinum oxidation at +250 mV vs Pt (+450 mV vs Ag/AgCl; +1150 mV vs RHE) as shown clearly in Fig. 18b.

2) DB Potentiostat Measurements: Chronoamperometric measurements with the DB potentiostat were performed in five solutions. The measurement setup in Fig. 15b is used for non-enzymatic glucose detection since the reaction peak voltage in Fig. 18b is within the common mode input range of the FI-DIGOTA [31] and thus, no external regulated DC voltages are needed. The clock frequency value has been kept equal to f_{clk} = 50 kHz while the static FI-DIGOTA currents have been set equal to i_{p} = 4.89 nA and i_{n} = 10.16 nA.

It has been found that the H1-ePt surface exhibits two approximately linear response regions over the 2 mM–50 mM glucose concentration range. The low-concentration branch shows the highest differential sensitivity, about 0.3 nA mM^{-1},

TABLE V: Potentiostats State-of-Art performance comparison

	Units	[13]	[17]	[22]	[28]	[29]	[30]	[32]	This Work		
Topology	-	I-V (R-TIA)	(C-TIA)	CC	I-F	DB	Digital	DB	DB		
Sensing Method	CV, CA	CA	CV, CA	CV, CA	CA	CA	CA	CA	CA		
Technology	nm	180	180	180	180	180	180	180	130		
Supply Voltage	V	1.8	1.8	1.5	1.2	0.4	1 - 1.8	0.4	0.3[a]	0.4[b]	0.5[c]
clk Frequency	kHz	-	5000	-	-	50	0.1 - 10000	25	50		
Power	nW	22000	86400	2330000	1400	4.7	3.72	1.2	1.65	2.96	53.5
Area	mm^2	0.0179	1.47	0.0684	0.037	0.00046	0.165	0.00026	0.011532		
Sensing Current Range	nA	$\pm$ 10 $\cdot 10^3$	(1 , 10$\cdot 10^3$)	(4.2$\cdot 10^3$, 180$\cdot 10^3$)	$\pm$2$\cdot 10^3$	(-22 , 33)	(0.08 , 240$\cdot 10^3$)	(-12 , 24)	(0.6 , 5.4)[d]	(4 , 180)[d]	(150 , 650)[d]
Input noise current	pA_{rms}	690 $\cdot 10^3$	0.16	-	26.5	65	50 $\cdot 10^3$	33	5.60	46.72	347.03
Dynamic Range	dB	155.92	131.4	-	-	58	129.5	60	59.68	71.72	65.45
Linearity	R^2	0.999	-	0.9	0.997	0.999	0.998	0.991	0.991		
Measurements	-	Yes	Yes	Yes	Yes	No	Yes	Yes	Yes		
Targeted Analyte	-	Glucose (e)	Dopamine	Glucose (e)	pH, Glucose (e)	Glucose (ne)	Glucose (e)	Dopamine	Glucose (ne)		

[a] calN = 1 (i_n = 10.16 nA), calP = 3 (i_p = 4.89 nA), [b] calN = 3 (i_n = 393 nA), calP = 12 (i_p = 276 nA), [c] calN = 1 (i_n = 1076 nA), calP = 3 (i_p = 660 nA), [d] i_{min} refers to the minimum measured current; it is not a limitation of the circuit.

while the response progressively decreases at higher concentrations, as shown in Fig. 19. The estimated limit of detection (LoD) is 530 µM, corresponding to 9.5 mg/dL.

The selectivity of the analyte is tested introducing 0.5 mM of L-ascorbic acid (AA) in the measured glucose solution, to simulate typical concentration of the interfering analyte. Fig. 20 shows the chronoamperometry of the 50 mM glucose solution with and without L-AA, demonstrating a negligible contribution of the interfering analyte in the overall reaction current thanks to the selectivity of the nanostructurated microelectrode. This is confirmed by the chronoamperometry tests performed in the presence of the interferent, which measure the same current in both cases. In particular, the measurement performed with the DB potentiostat with and without the interfering analyte presents a relative error of 0.02%.

Longer-term operation in PBS and in complex biological media may be affected by Pt surface poisoning, oxide formation, nonspecific adsorption and drift; these effects are outside the scope of the present proof-of-concept validation and will require dedicated stability studies.

B. Potentiostat SoA Comparison

The comparison with the state of the art (SoA) for IC potentiostats is presented in TableV. It is evident that digital potentiostats [29] [30] [32] drastically reduce the power consumption with respect to standard topology even if the applicability of this strategy is still limited, and CV can not be performed.

Despite the area overhead due to the trimmable output stage, the overall area is still smaller than other non-DB potentiostats, and the degrees of freedom (V_{DD}, cal and f_{clk}) entailed by the presented DB potentiostat allow to sense a wide electrochemical current range maintaining a minimum power consumption and the value of the supply voltage equal or lower than 500 mV. Furthermore, the clock frequency value can be decreased to further reduce the power consumption at the expense of current resolution.

VIII. Conclusions

In this paper an ULV, ULP chronoamperometric electrochemical sensor based on a configurable DB-potentiostat in 130 nm has been designed and experimentally characterized, revealing the detection of a wide electrochemical current range, spanning from 600 pA to 650 nA, with R^2=0.991 linearity at only 1.65 nW (53.5 nW) power consumption at V_{DD} = 300 mV (V_{DD} = 500 mV). The signal transfer and noise characteristics of the DB-potentiostat have been analytically described in the frequency domain for the first time and validated by simulations and experiments.

Then, a nanostructured mesoporous electrode has been specifically co-designed to operate with the DB-potentiostat in an ULV/ULP sensor for non-enzymatic glucose detection. The sensing platform consisting of the DB potentiostat and the electrode has been first validated both under diffusion-controlled regime and then under kinetic-controlled regime for the target glucose monitoring application, demonstrating, for the first time, successful non-enzymatic glucose detection at physiological levels at the lowest reported power (1.65 nW) and at the lowest reported supply voltage (0.3 V), thus revealing a strong potential for emerging PoC diagnostics applications.

References

[1] J. Kim, A. S. Campbell, B. E. F. de Ávila, and J. Wang, "Wearable biosensors for healthcare monitoring," *Nature Biotechnology*, vol. 37, pp. 389–406, 2019.

[2] Y. Qu, I. Yakub, R. Baini, W. Hu, and L. Wang, "Ag+ colorimetric sensor based on graphene oxide/nano-platinum composite," *Journal of Analytical Science and Technology*, vol. 14, 08 2023.

[3] B. Aguilera-Venegas, C. Olea-Azar, V. J. Arán, J. D. Maya, U. Kemmerling, H. Speisky, and F. Mendizábal, "Electrochemical, esr and theoretical insights into the free radical generation by 1,1'-hydrocarbylenebisindazoles and its evaluation as potential bio-active compounds," *International Journal of Electrochemical Science*, vol. 7, no. 7, pp. 5837–5863, 2012.

[4] I. Kocak and F. Pekdemir, "Non-enzymatic electrochemical detection of hydrogen peroxide and glucose through using copper(ii) and platinum(ii) complexes with tridentate ligand – platinum nanoparticles – graphene oxide composite," *Journal of The Electrochemical Society*, vol. 170, p. 066501, jun 2023.

[5] Y. Wang, H. Guo, M. Yuan, J. Yu, Z. Wang, and X. Chen, "One-step laser synthesis platinum nanostructured 3d porous graphene: A flexible dual-functional electrochemical biosensor for glucose and ph detection in human perspiration," *Talanta*, vol. 257, p. 124362, 2023.

[6] S. Carrara, *Bio/CMOS Interfaces and Co-Design*. Springer, 2013.

[7] S. Lee, J. Lee, S. Park, H. Boo, H. C. Kim, and T. D. Chung, "Disposable non-enzymatic blood glucose sensing strip based on nanoporous platinum particles," *Applied Materials Today*, vol. 10, pp. 24–29, 2018.

[8] A. Niyazi, A. Linden, and M. Di Lorenzo, "Robust pt/au composite nanostructures for abiotic glucose sensing," *Biosensors*, vol. 15, p. 588, 2025.

[9] Y.-J. Kim, S. R. Chinnadayyala, H. T. N. Le, and S. Cho, "Sensitive electrochemical non-enzymatic detection of glucose based on wireless data transmission," *Sensors*, vol. 22, p. 2787, 2022.

[10] M. Alioto, *Enabling the Internet of Things—From Integrated Circuits to Integrated Systems*. Cham, Switzerland: Springer, 2017.

[11] M. Alioto, "From less batteries to battery-less: Enabling a greener world through ultra-wide power-performance adaptation down to pws," in *ESSCIRC 2022- IEEE 48th European Solid State Circuits Conference (ESSCIRC)*, pp. 33–40, 2022.

[12] L. Dong, S. Ren, X. Zhang, Y. Yang, Q. Wu, and T. Lei, "In-situ synthesis of pt nanoparticles/reduced graphene oxide/cellulose nanohybrid for nonenzymatic glucose sensing," *Carbohydrate Polymers*, vol. 303, p. 120463, 2023.

[13] K. A. Al Mamun, S. K. Islam, D. K. Hensley, and N. McFarlane, "A glucose biosensor using cmos potentiostat and vertically aligned carbon nanofibers," *IEEE Transactions on Biomedical Circuits and Systems*, vol. 10, no. 4, pp. 807–816, 2016.

[14] Q. Lin, W. Sijbers, C. Avdikou, D. Gomez, D. Biswas, S. Sneha, A. Malissovas, B. Tacca, and N. Van Helleputte, "21.2 a 22μW peak power multimodal electrochemical sensor interface ic for bioreactor monitoring," in *2023 IEEE International Solid-State Circuits Conference (ISSCC)*, pp. 314–316, 2023.

[15] D. Djekic, G. Fantner, K. Lips, M. Ortmanns, and J. Anders, "A 0.1% thd, 1-m ω to 1-g ω tunable, temperature-compensated transimpedance amplifier using a multi-element pseudo-resistor," *IEEE Journal of Solid-State Circuits*, vol. 53, no. 7, pp. 1913–1923, 2018.

[16] A. Yasar, D. Caygara, Y. H. Patel, A. Pemaraj, L. Boisvert, A. Magyar, T. Yu, B. Dufort, T.-L. Poo, and R. T. Yazicigil, "A secure multimodal electrochemical sensor for sustainable biomanufacturing," in *2025 IEEE European Solid-State Electronics Research Conference (ESSERC)*, pp. 413–416, 2025.

[17] M. Chilukuri, S. Lakshminarayana, H. Park, C. Pan, H.-J. Chung, and S. Jung, "A low-noise, low-offset cmos readout ic for amperometric biosensors," *IEEE Access*, vol. 12, pp. 180619–180630, 2024.

[18] S. S. Ghoreishizadeh, I. Taurino, G. De Micheli, S. Carrara, and P. Georgiou, "A differential electrochemical readout asic with heterogeneous integration of bio-nano sensors for amperometric sensing," *IEEE Transactions on Biomedical Circuits and Systems*, vol. 11, no. 5, pp. 1148–1159, 2017.

[19] C.-L. Hsu and D. A. Hall, "A current-measurement front-end with 160db dynamic range and 7ppm inl," in *2018 IEEE International Solid-State Circuits Conference - (ISSCC)*, pp. 326–328, 2018.

[20] Z. Wang, X. Liu, Z. Liu, J. Zhang, and T. Fang, "A continuous blood glucose monitoring front end ic design with large input range," in *2023 8th International Conference on Integrated Circuits and Microsystems (ICICM)*, pp. 128–133, 2023.

[21] V. Valente, N. Neshatvar, E. Pilavaki, M. Schormans, and A. Demosthenous, "1.2-v energy-efficient wireless cmos potentiostat for amperometric measurements," *IEEE Transactions on Circuits and Systems II: Express Briefs*, vol. 67, no. 10, pp. 1700–1704, 2020.

[22] R. Ahmad, A. M. Joshi, and D. Boolchandani, "Programmable readout with integrated bandgap reference potentiostat for glucose sensing," *IEEE Transactions on Instrumentation and Measurement*, vol. 73, pp. 1–11, 2024.

[23] H. Li, C. S. Boling, and A. J. Mason, "Cmos amperometric adc with high sensitivity, dynamic range and power efficiency for air quality monitoring," *IEEE Transactions on Biomedical Circuits and Systems*, vol. 10, no. 4, pp. 817–827, 2016.

[24] C. I. Dorta-Quiñones, X. Y. Wang, R. K. Dokania, A. Gailey, M. Lindau, and A. B. Apsel, "A wireless fscv monitoring ic with analog background subtraction and uwb telemetry," *IEEE Transactions on Biomedical Circuits and Systems*, vol. 10, no. 2, pp. 289–299, 2016.

[25] S. Kang, B. Jin, M. Yoo, H. Son, K. Kim, J. Wi, G. Nam, N. Ho Bae, Y. Min Park, J. Ho Jang, and H. Ko, "Low-noise and process variation-tolerant readout circuit for electrochemical sensors," *IEEE Sensors Journal*, vol. 24, no. 12, pp. 19274–19285, 2024.

[26] S. Yu, T.-H. Chou, S. Bose, J. Cook, J. Park, and M. L. Johnston, "A reconfigurable tri-mode frequency-locked loop readout circuit for biosensor interfaces," *IEEE Transactions on Biomedical Circuits and Systems*, vol. 17, no. 4, pp. 768–781, 2023.

[27] F.-T. Lin, S.-Y. Lu, and Y.-T. Liao, "A 2.2 μW, -12 dbm rf-powered wireless current sensing readout interface ic with injection-locking clock generation," *IEEE Transactions on Circuits and Systems I: Regular Papers*, vol. 63, no. 7, pp. 950–959, 2016.

[28] T.-H. Chou, S. Yu, S. Bose, J. Cook, J. Park, and M. L. Johnston, "Wireless, multi-sensor system-on-chip for ph and amperometry powered by body heat," *IEEE Transactions on Biomedical Circuits and Systems*, vol. 17, no. 4, pp. 782–794, 2023.

[29] R. Rubino, S. Carrara, and P. Crovetti, "Direct digital sensing potentiostat targeting body-dust," in *2022 IEEE Biomedical Circuits and Systems Conference (BioCAS)*, pp. 280–283, 2022.

[30] M. A. Akram, A. Aberra, S.-J. Kweon, and S. Ha, "An ultra-low-power amplifier-less potentiostat design based on digital regulation loop," *IEEE Transactions on Biomedical Circuits and Systems*, vol. 19, no. 5, pp. 993–1004, 2025.

[31] A. De Gregorio, D. K. Kaddouri, G. Bosisio, P. Angelini, G. Bruno, and P. S. Crovetti, "Programmable floating inverter-based digital ota for electrochemical biosensing," in *2025 20th International Conference on PhD Research in Microelectronics and Electronics (PRIME)*, pp. 1–4, 2025.

[32] A. Meimandi, G. L. Barbruni, P. S. Crovetti, and S. Carrara, "Sub- 9 $\times$ 29 μm^2, 1.2nw, fully digital potentiostat design for dopamine sensing," *IEEE Sensors Journal*, vol. 25, no. 20, pp. 38792–38799, 2025.

[33] P. S. Crovetti, "A digital-based analog differential circuit," *IEEE Transactions on Circuits and Systems I: Regular Papers*, vol. 60, no. 12, pp. 3107–3116, 2013.

[34] P. Toledo, P. Crovetti, O. Aiello, and M. Alioto, "Design of digital otas with operation down to 0.3 v and nw power for direct harvesting," *IEEE Transactions on Circuits and Systems I: Regular Papers*, vol. 68, no. 9, pp. 3693–3706, 2021.

[35] G. S. Attard, P. N. Bartlett, N. R. B. Coleman, J. M. Elliott, J. R. Owen, and J. H. Wang, "Mesoporous platinum films from lyotropic liquid crystalline phases," *Science*, vol. 278, no. 5339, pp. 838–840, 1997.

[36] J. M. de la Rosa, "Sigma-delta modulators: Tutorial overview, design guide, and state-of-the-art survey," *IEEE Transactions on Circuits and Systems I: Regular Papers*, vol. 58, no. 1, pp. 1–21, 2011.

[37] W. Franks, I. Schenker, P. Schmutz, and A. Hierlemann, "Impedance characterization and modeling of electrodes for biomedical applications," *IEEE Transactions on Biomedical Engineering*, vol. 52, no. 7, pp. 1295–1302, 2005.

[38] J. M. Elliott and J. R. Owen, "Electrochemical impedance characterisation of a nanostructured (mesoporous) platinum film," *Phys. Chem. Chem. Phys.*, vol. 2, pp. 5653–5659, 2000.

[39] E. Klumperink, S. Gierkink, A. van der Wel, and B. Nauta, "Reducing mosfet 1/f noise and power consumption by switched biasing," *IEEE Journal of Solid-State Circuits*, vol. 35, no. 7, pp. 994–1001, 2000.

[40] Y. B. Vassilyev, O. A. Khazova, and N. N. Nikolaeva, "Kinetics and mechanism of glucose electrooxidation on different electrode-catalysts: Part i. adsorption and oxidation on platinum," *Journal of Electroanalytical Chemistry and Interfacial Electrochemistry*, vol. 196, no. 1, pp. 105–125, 1985.

[41] Y. B. Vassilyev, O. A. Khazova, and N. N. Nikolaeva, "Kinetics and mechanism of glucose electrooxidation on different electrode-catalysts: Part ii. effect of the nature of the electrode and the electrooxidation mechanism," *Journal of Electroanalytical Chemistry and Interfacial Electrochemistry*, vol. 196, no. 1, pp. 127–144, 1985.

[42] A. Khamsavi, Y. Abdi, and M. Z. Meymian, "A novel two-electrode nonenzymatic electrochemical glucose sensor based on vertically aligned carbon nanotube arrays," *IEEE Sensors Letters*, vol. 3, no. 3, pp. 1–4, 2019.

[43] I. Taurino, G. Sanzò, F. Mazzei, A. Tino, S. Scarano, M. Staiano, W. Porzio, and S. D'Auria, "Fast synthesis of platinum nanopetals and nanospheres for highly-sensitive non-enzymatic detection of glucose and selective sensing of ions," *Scientific Reports*, vol. 5, p. 15277, 2015.

[44] D. Pletcher, R. Greff, R. Peat, L. Peter, and J. Robinson, *Instrumental Methods in Electrochemistry*. Chemical Science, Woodhead Publishing, 2001.

[45] M. Fleischmann and S. Pons, "The behavior of microelectrodes," *Analytical Chemistry*, vol. 59, no. 24, pp. 1391A–1399A, 1987.

[46] S. A. G. Evans, J. M. Elliott, L. M. Andrews, P. N. Bartlett, P. J. Doyle, and G. Denuault, "Detection of hydrogen peroxide at mesoporous platinum microelectrodes," *Analytical Chemistry*, vol. 74, no. 6, pp. 1322–1326, 2002.

[47] M. Serrapede, G. Denuault, M. Sosna, G. L. Pesce, and R. J. Ball, "Scanning electrochemical microscopy: Using the potentiometric mode of secm to study the mixed potential arising from two independent redox processes," *Analytical Chemistry*, vol. 85, no. 17, pp. 8341–8346, 2013.

[48] C. I. Gho, M. Serrapede, K. Bejtka, M. Fontana, P. Zaccagnini, A. Lamberti, F. C. Pirri, G. Denuault, and A. Chiodoni, "Nanostructured palladium electrodes for reliable confined electrochemistry: impact on electrochemical liquid-phase tem," *ChemRxiv*, vol. 2026, no. 0426, 2026.

[49] S. Trasatti and O. Petrii, "Real surface area measurements in electrochemistry," *Journal of Electroanalytical Chemistry*, vol. 327, no. 1, pp. 353–376, 1992. An International Journal Devoted to all Aspects of Electrode Kinetics, Interfacial Structure, Properties of Electrolytes, Colloid and Biological Electrochemistry.

[50] T. Biegler, D. Rand, and R. Woods, "Limiting oxygen coverage on platinized platinum; relevance to determination of real platinum area by hydrogen adsorption," *Journal of Electroanalytical Chemistry and Interfacial Electrochemistry*, vol. 29, no. 2, pp. 269–277, 1971.
[51] M. Alioto, "Ultra-low power vlsi circuit design demystified and explained: A tutorial," *IEEE Transactions on Circuits and Systems I: Regular Papers*, vol. 59, pp. 3–29, Jan. 2012.
[52] R. Della Sala, M. Privitera, G. Scotti, A. D. Grasso, and M. Alioto, "Two-stage inverter-based ota with 56-db gain and digitally reconfigurable gbw/sr for pvt-resiliency," *IEEE Transactions on Circuits and Systems I: Regular Papers*, vol. 73, no. 4, pp. 2227–2239, 2026.
[53] T. F. Esterle, A. E. Russell, and P. N. Bartlett, "Study of carbon monoxide oxidation on mesoporous platinum," *ChemPhysChem*, vol. 11, no. 13, pp. 2896–2905, 2010.
[54] P. J. Mahon and K. B. Oldham, "Diffusion-controlled chronoamperometry at a disk electrode," *Analytical Chemistry*, vol. 77, no. 18, pp. 6100–6101, 2005.

Andrea De Gregorio received the B.S. and M.S. degrees in electronic engineering from Politecnico di Torino, Turin, Italy, in 2021 and 2023, respectively. He is currently pursuing the Ph.D. degree with the Analog, Mixed-Signal, and Power Electronics Group in the Department of Electronics and Telecommunications at the same institution. His research focuses on the design and characterization of ultra-low-voltage, ultra-low-power integrated front ends for electrochemical biosensors.

Mara Serrapede is Assistant Professor (RTdA) in Experimental Physics of Matter at the Politecnico di Torino and affiliated with the Istituto Italiano di Tecnologia. She graduated in 2010 at the Università di Torino and obtained her PhD in Electrochemistry in 2014 at the University of Southampton. She is the author of several patents with industrial parteners and international publications in the field of electrochemical materials, stationary and flexible energy storage devices, operando electrochemistry and sensors. She has contributed to national and international research projects on energy conversion and storage technologies.

Danilo Karim Kaddouri received the the MSc degree with honors in electronic engineering from Politecnico di Torino, Turin, Italy in 2011 with a Thesis on the EMI Susceptibility of the Pierce Oscillator. Since 2012, he has been with STMicroelectronics, where he has worked as analog integrated circuit designer engineer, initially in a MEMS sensor front – end design group and now in a R&D advanced design group. Among his principal interests are the design of analog continuous–time amplifiers and filters, bandgap references and oscillators.

Paolo Angelini received the Laurea degree in electronic engineering from the University of Bologna, Bologna, Italy, in 2007. In 2007, he joined STMicroelectronics, where he was analog designer for MEMS sensor front-end design. From 2015, he moved to the STMicroelectronics AMS group Central R&D organization, and he is currently leading a team of advanced analog design.

Giuseppe Bruno received the degree in electronic engineering from the University of Palermo, Italy, in 1994. In 1995, he joined STMicroelectronics, where he was involved in the design of power bipolar transistors. From 1998 to 2007, he served as Cellular Front-End Module Design Manager, focusing on the development of fully integrated power amplifier modules for GSM/WCDMA mobile handsets. Since 2010, he has been an Innovation Product Design Manager within the ST AMS (Analog MEMS and Sensor) R&D organization, with main interests in environmental and optical MEMS sensors and bio-potential acquisition systems. He has authored/coauthored several conference and journal papers and holds several patents.

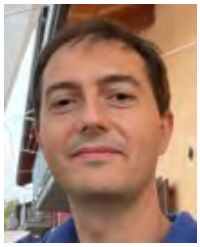

Simone Luigi Marasso is Senior Researcher at CNR-IMEM and he is responsible for the research activities at the operative unit at the Politecnico di Torino. He received his master's degree in Biomedical Engineering from Politecnico di Torino in 2005. After obtaining his PhD in Electronic Devices in 2010, he conducted a Postdoctoral Research Fellowship and he worked in Chilab, materials and microsystem laboratory of Politecnico di Torino, Chivasso (TO), Italy. Since 2018, he is involved in the foundation of the Piemonte Quantum Enabling Technology LAB, Piquet Lab (https://piquetlab.it) and he is currently member of the cleanroom operative committee. His research is focused mainly on Lab on a Chip, Organ on a Chip and biosensors.

Salvatore Guastella is currently responsible of the microscopy laboratory at the Politecnico di Torino. He obtained his Master's degree in Electronic Engineering from the Politecnico di Torino in 2002. After receiving his PhD in Physics in 2008, he has conducted research involving the characterization of various types of samples for projects spanning both fundamental and applied research (with significant industrial involvement); this work includes FESEM (Field Emission Scanning Electron Microscopy) and TEM (Transmission Electron Microscopy) imaging, as well as the measurement, analysis, and interpretation of XPS (X-ray Photoelectron Spectroscopy) spectra.

Andrea Lamberti is Full Professor of Experimental Physics of Matter at the Politecnico di Torino. He graduated in 2009 in Physical Engineering at the Politecnico di Torino and obtain the PhD in Electronic Devices in 2013 working in the Italian Institute of Technology. He is the author of over 200 publications and several book chapters and patents in the field of nanomaterials for energy harvesting and storage devices. He has contributed significantly to projects on electrochemical energy devices which have led to numerous European and national projects.

Paolo Stefano Crovetti (Senior Member, IEEE) was born in Turin, Italy, in 1976. He received the Laurea degree (summa cum laude) and the Ph.D. degree in electronic engineering from Politecnico di Torino, Turin, Italy, in 2000 and 2003, respectively. He is currently an Associate Professor with the Department of Electronics and Telecommunications, Politecnico di Torino, where he leads a research group working on analog, mixed-signal, and power microelectronics in collaboration with academic and industrial partners worldwide. He has co-authored more than 120 papers published in international journals and conference proceedings. His recent research interests include nonconventional digital-based analog information processing and ultra-low-voltage, ultra-low-power integrated analog interfaces for energy-autonomous biosensors and Internet of Things sensor nodes. He is the principal investigator of MicroBioNIC, a research project funded by the Italian Ministry of University and Research and focused on microscale biosensing applications. Prof. Crovetti was a co-recipient of the Excellent Paper Award at the 2009 International Symposium on Electromagnetic Compatibility, Kyoto, and the Best Student Paper Award at the 2019 IEEE International Conference on Electronics, Circuits and Systems. He is currently the Editor-in-Chief of IET Electronics Letters and serves as a Senior Associate Editor for IEEE Transactions on Circuits and Systems—I: Regular Papers and for IEEE Transactions on Very Large Scale Integration (VLSI) Systems. From 2024 to 2025, he served as Co-Chair of the IEEE Electromagnetic Compatibility Society Italy Chapter.